Sierpiński Structure and Electronic Topology in Bi Thin Films on InSb(111)B Surfaces

Chen Liu,[1] Yinong Zhou,[2] Guanyong Wang,[3] Yin Yin,[1] Can Li,[1] Haili Huang,[1] Dandan Guan,[1,4] Yaoyi Li,[1,4] Shiyong Wang,[1,4] Hao Zheng,[1,4] Canhua Liu,[1,4] Yong Han,[5,6,*] James W. Evans,[5,6] Feng Liu,[2] and Jinfeng Jia[1,4,†]

[1]*Key Laboratory of Artificial Structures and Quantum Control (Ministry of Education), Shenyang National Laboratory for Materials Science, School of Physics and Astronomy, Shanghai Jiao Tong University, Shanghai 200240, China*

[2]*Department of Materials Science and Engineering, University of Utah, Salt Lake City, Utah 84112, USA*

[3]*Shenzhen Institute for Quantum Science and Engineering, Southern University of Science and Technology, Shenzhen 518055, China*

[4]*Tsung-Dao Lee Institute, Shanghai Jiao Tong University, Shanghai 200240, China*

[5]*Department of Physics and Astronomy, Iowa State University, Ames, Iowa 50011, USA*

[6]*Ames Laboratory, U.S. Department of Energy, Ames, Iowa 50011, USA*

(Received 27 November 2020; revised 11 February 2021; accepted 19 March 2021; published 30 April 2021)

Deposition of Bi on InSb(111)B reveals a striking Sierpiński-triangle (ST)-like structure in Bi thin films. Such a fractal geometric topology is further shown to turn off the intrinsic electronic topology in a thin film. Relaxation of a huge misfit strain of about 30% to 40% between Bi adlayer and substrate is revealed to drive the ST-like island formation. A Frenkel-Kontrova model is developed to illustrate the enhanced strain relief in the ST islands offsetting the additional step energy cost. Besides a sufficiently large tensile strain, forming ST-like structures also requires larger adlayer-substrate and intra-adlayer elastic stiffnesses, and weaker intra-adlayer interatomic interactions.

DOI: 10.1103/PhysRevLett.126.176102

The Sierpiński triangle (ST) [1] is a self-similar fractal with a fractional Hausdorff dimension $d_H = \log_2 3 = 1.584\,96\cdots$ and with fascinating mathematical properties [2]. Historically, such beautiful patterns were often utilized for aesthetic reasons, especially in architecture, e.g., on the medieval floors in Rome [3]. Many fundamental and intriguing phenomena in ancient and modern mathematics and physics, as well as computer science, are related to the STs, such as Pascal triangles [4], towers of Hanoi [5], chaos games [6], cellular automata [7], DNA computing [8,9], etc.

Theory and experiment have shown that fractal materials can exhibit plentiful and unusual thermal, mechanical, electric, electronic, electromagnetic, and optical properties which are often desirable for prospective nanodevice applications [10–16]. Fractal quasicrystals have even been predicted to possess nontrivial electronic topology usually pertained to crystals [17,18]. Recently, there has been also considerable interest in fabricating ST-like fractal materials, although the synthesis of such systems is notoriously difficult [19]. In 2014, a terpyridine-based architecture mimicking ST was synthesized in solution [20]. Subsequently, several research groups have successfully fabricated the fractal supramolecular materials featuring the ST pattern on the coinage metal surfaces: Ag(111) [21], Ag(100) [22], Au(111) [23–28], Au(100) [28,29], and Cu(111) [30], as well as on a graphite surface [31]. These fabricated fractal supramolecules can be organic, metal organic, CO compounds, etc., [16]. Theoretically, Monte Carlo simulations show that the formation of molecular STs in these systems is essentially related to directional intermolecular bonds [32,33].

As indicated above, previous fabrication of STs in experiments is by assembling small carbon-based molecules into supramolecules. There has not yet been any report of the synthesis for STs composed of single-element atoms. Obviously, experimental fabrication of such pure single-element STs is more challenging without the specifically shaped tectons providing directional intermolecular interactions [32,33]. In this work, by depositing Bi atoms on an InSb(111)B surface around 400 K, we have observed ST-like Bi films with a thickness of one to three monatomic layers (MLs) from our scanning-tunneling-microscope (STM) experiments. Our proposed theoretical model reveals that the formation of a Bi ST island requires an unusually large lattice mismatch between a monatomic Bi adlayer and substrate, relatively large adlayer-substrate and intra-adlayer elastic stiffnesses, and relatively weak intra-adlayer interatomic interactions. This formation mechanism essentially differs from that of the supramolecular STs synthesized previously.

In addition, it has been predicted theoretically that an ultrathin Bi film exhibits a stable nontrivial topological property [34–36], which makes the investigations of heteroepitaxial growth of ultrathin Bi films fundamentally interesting. Experiments have demonstrated the existence

of nontrivial topological edge states of single Bi(111) bilayer grown on Bi_2Te_3 films [37], as well as coexistence of topological edge state and superconductivity of Bi(111) ultrathin film grown on the $NbSe_2$ superconducting substrate [38]. Theoretical prediction of high-temperature quantum-spin-Hall state in an epitaxial Bi layer (called "bismuthene") grown on semiconductor substrates [39–41] has been recently confirmed experimentally for a SiC substrate [42]. A possible realization of topological high-temperature superconductivity in a hybrid of Bi(110) ultrathin film and copper oxide superconductor has been also reported recently [43]. Therefore, it is of interest to assess if the electronic topology is retained in ST Bi films.

The most common phase of a Bi bulk crystal is the α-As structure, the geometric parameters for which and Bi(111) film surface structure are shown in Supplemental Material, Fig. S1 [44]. Bulk InSb has a zinc blende structure. An InSb(111) surface with In termination is often called InSb(111)A surface, while an InSb($\bar{1}\,\bar{1}\,\bar{1}$) surface with Sb termination is often called InSb(111)B surface. The structure parameters for bulk InSb and (111) surfaces are shown in Fig. S2. An InSb(111)B surface can exhibit (3×3), (2×2), or (3×1) reconstruction, depending on the experimental conditions [58–65]. In our experiments, a smooth InSb(111)B surface is produced following an ultrahigh-vacuum (UHV) cleaning process (see Supplemental Material, Sec. S1 for details [44]). STM, reflection high-energy electron diffraction (RHEED), and two-dimensional fast-Fourier-transform (2D FFT) measurements indicate that the InSb(111)B surface is (3×3) reconstructed (see Supplemental Material, Fig. S3 [44]). For the (3×3)-reconstructed InSb(111)B surface, a currently accepted model is that proposed by Wever *et al.* in 1994, where the reconstructed top layer was determined to be composed of three types of In-Sb hexamers: α, β, and γ rings, from their x-ray diffraction and STM analyses [61]. This model also reasonably agrees with other experimental observations [60,64,65]. These conclusions are generally consistent with our STM results in Fig. S3 [44].

In our experiments, we deposit Bi atoms to a desired coverage θ (in units of ML; see Sec. S1 [44]) on the prepared InSb(111)B substrate surface (as described above) at a temperature T_{dep}. After deposition, we quench the system to room temperature with a total cooling time of t_{cool}. We measure the STM images at the liquid helium temperature of about 4 K. For more STM measurement details, see Sec. S1 [44].

The STM images in Figs. 1(a) and 1(b) show typical ST-like Bi films or islands formed on InSb(111)B surface at $\theta \approx 2$ ML, where different island height levels: 0, S_1, 2, S_3, 4, and B from lower to higher, are labeled. For a clearer view, these levels are plotted into a schematic in Fig. 1(c). Corresponding to the blue, red, and pink lines A, B, and C in Fig. S1(b) [44], the height profiles are shown in Figs. 1(d)–1(f), respectively. Level 0 is assumed to be a wetting layer composed of Bi, Sb, and In atoms by considering the (3×3) reconstruction of InSb(111)B surface (as described above) before deposition. As analyzed below, level S_1 corresponds to a ST-like 1-ML Bi on the wetting layer, level 2 to a 2-ML Bi, and level S_3 to a ST-like 1-ML Bi on 2-ML Bi. From our STM measurements (e.g., see Fig. 2, and Supplemental Material Figs. S4–S6 [44]), the regions of level 2 are (2×2)-reconstructed or disordered (see Sec. S3.5 [44]). Level 4 has a low occurrence statistically and is expected to be of 4-ML Bi (see analyses below). We label the higher bulklike islands than level 4 as level B.

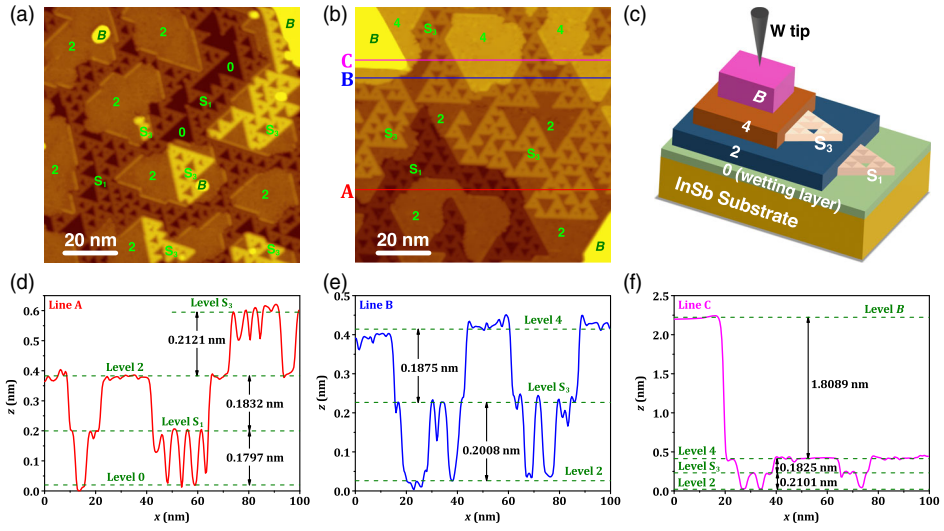

FIG. 1. (a),(b) STM images of typical ST-like Bi islands formed on InSb(111)B substrate at $\theta \approx 2$ ML. See Sec. S1 for details. (c) Schematic for different island height levels corresponding to the labels in (a),(b). (d),(e),(f) Height profiles for red, blue, and pink lines A, B, and C in (b), respectively.

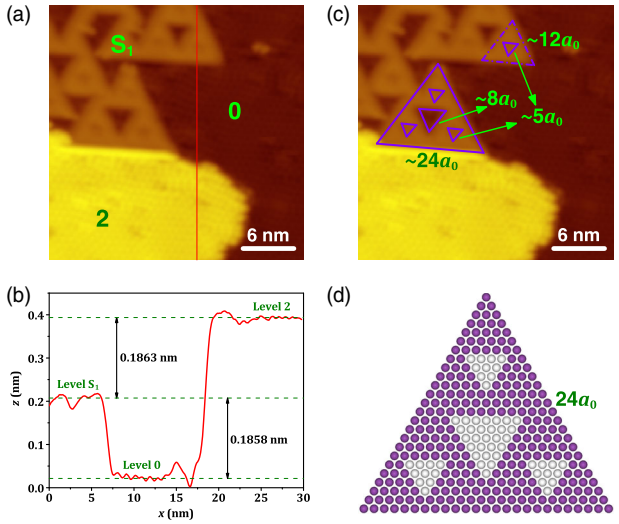

FIG. 2. (a) STM image at $\theta \approx 1$ ML. See Supplemental Material, Sec. S1 [44] for details. (b) Height profile for a red line in (a). (c) The same image as (a). Side lengths of STs are indicated. (d) Atomistic structure model for a 1-ML Bi ST with all side lengths accurately matching the lengths measured in (c). A purple ball denotes a lattice site occupied by a Bi atom and a gray ball denotes an unoccupied lattice site.

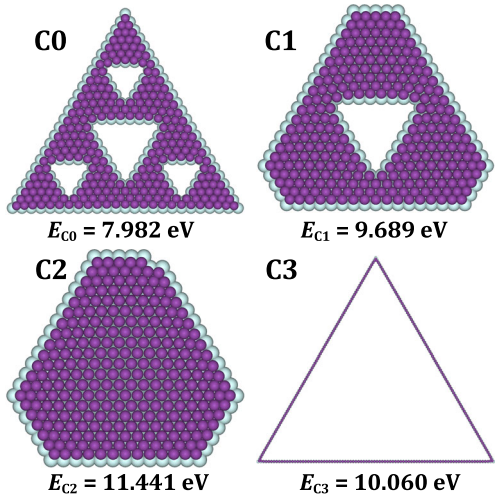

FIG. 3. Shapes and energies of four configurations after energy minimization for 1-ML Bi islands with the same number of Bi atoms, $N = 267$. A purple ball represents a Bi atom and a light ball represents a lattice point below this Bi atom. For $C0$, $C1$, and $C2$, $b = b_{1\,\mathrm{ML}} = 0.3304$ nm, $k_2 = k_{1\,\mathrm{ML}} = 766$ eV/nm^2, and $\phi = \phi_{1\,\mathrm{ML}} = -0.747$ eV; for $C3$, $b = b_{\mathrm{chain}} = 0.2865$ nm, $k_2 = k_{\mathrm{chain}} = 814$ eV/nm^2, and $\phi = \phi_{\mathrm{chain}} = -1.638$ eV; for all, $l = a_0 = 0.45816$ nm and $k_1 = k_{\mathrm{sub}} = 307$ eV/nm^2.

To model the atomistic structure of ST-like islands, we measure various side lengths of STs. The measured typical STs are shown in Fig. 2(a), where $\theta \approx 1$ ML. There are three height levels for this coverage, as shown by the line scan in Fig. 2(b). The height differences from level 0 to S_1 or from S_1 to 2 are about 0.186 nm, which is consistent with the values around 0.18 nm at $\theta \approx 2$ ML in Fig. 1(d). In Fig. 2(c), we highlight various side lengths of STs by purple lines, e.g., for a large ST, three longest side lengths are about $24a_0$ and the three side lengths of the inner larger vacancy triangle are about $8a_0$, while each of side lengths of three inner smallest vacancy triangles are about $5a_0$, where $a_0 = 0.458\,16$ nm is the InSb(111) plane lattice constant from experiments [66–68]. For the dashed triangle, each side length is about $12a_0$. That is, all these side lengths are approximately equal to integer multiples of a_0. Thus, a model for the atomistic structure of a ST Bi island can be obtained with the side lengths which can accurately match our experimental measurements, as illustrated in Fig. 2(d). Here, it should be also noted that the above side lengths are statistically representative values based on analysis of multiple STs from our STM images.

It is important to point out that the above STM analysis indicates that the nominal 1-ML Bi film has a huge lattice mismatch (>30%) with the substrate, as described below. Therefore, the film is unlikely to grow coherently rather forming extended defects to relieve strain. Instead of a normal mechanism of forming dislocations, islands, or voids [69,70], a novel unique strain relief mechanism via formation of ST-like structure is revealed, as elaborated below. Specifically, for a 1-ML Bi island with N Bi atoms on a substrate with a surface lattice parameter l, the total energy can be expressed as $E_{\mathrm{total}} = E_{\mathrm{electronic}} + E_{\mathrm{elastic}}^{\mathrm{Bi-sub}} + E_{\mathrm{elastic}}^{\mathrm{Bi-Bi}}$, based on a generic form of Frenkel-Kontrova-type Hamiltonian for elastic relaxations in bulk alloys [71] (for three terms, see Sec. S2.1 [44]). Considering the measured side lengths for STs in Fig. 2, we reasonably assume that the underlying InSb(111)B substrate has a triangular lattice with $l = a_0 = 0.458\,16$ nm at the interface. Other model parameters include spring parameters k_1 (adlayer-substrate) and k_2 (intra-adlayer), effective interaction parameter ϕ, and equilibrium adlayer lattice parameter b (see Sec. S2 [44]).

Consider four configurations with $N = 267$ in Fig. 3. $C0$ corresponds to the ST in Fig. 2(d). In principle, one can assess the thermodynamic stability of $C0$ by constructing a large number of configurations with the same N and then comparing their energies with $C0$ after energy minimization. However, analysis of just few judiciously selected configurations is sufficiently informative. We choose $C1$, $C2$, and $C3$. For $C1$, only the larger void in the middle remains relative to $C0$ and the three smaller voids around it are filled by truncating three ST edges to retain 267 atoms. For $C2$, we consider the limit of a compact island without any voids retaining 267 atoms. For $C3$, we consider the *opposite* limit to $C2$, where a single large void is bordered by three Bi monatomic chains. The energies of other configurations are expected to be between these limiting cases.

In contrast to $C3$, the configurations $C0$, $C1$, and $C2$ all involve portions of complete compact 1-ML Bi film.

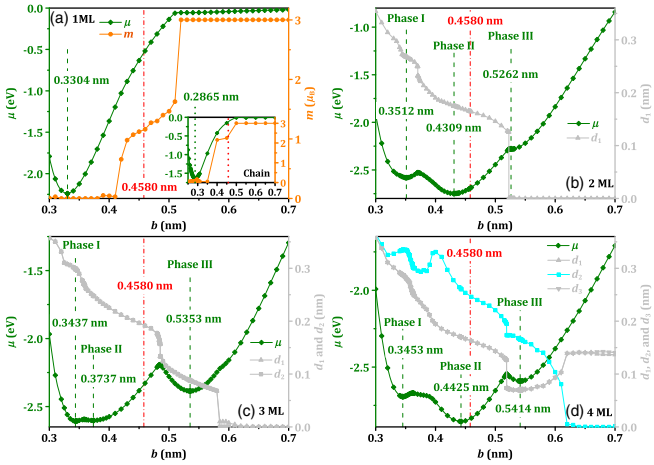

FIG. 4. DFT chemical potentials μ (the energy per Bi atom relative to gas phase) versus lateral lattice parameter b for freestanding (a) 1-, (b) 2-, (c) 3-, and (4) 4-ML Bi slabs. Interlayer spacings (d_1, d_2, and d_3) for 2-, 3-, and 4-ML slabs, as well as magnetic moments m for 1 ML in (a) and chain in the inset of (a), are also plotted. For details, see Sec. S3.2.

This motivates selecting the same set of parameters for them: $b = b_{1\,\mathrm{ML}} = 0.3304$ nm, $k_2 = k_{1\,\mathrm{ML}} = 766$ eV/nm^2, and $\phi = \phi_{1\,\mathrm{ML}} = -0.747$ eV. $b_{1\,\mathrm{ML}}$ is the DFT equilibrium lattice parameter for complete freestanding 1-ML Bi film [see Fig. 4(a)] and significantly less than a_0. Therefore, the nominal 1-ML Bi film has a huge tensile strain $\varepsilon = 38.67\%$ relative to a_0. $k_{1\,\mathrm{ML}}$ and $\phi_{1\,\mathrm{ML}}$ are estimated from our DFT calculations for the 1-ML Bi. $C3$ is made up of three monatomic Bi chains with an only slight deviation from the chain shape at each vertex, so we approximately take the parameters to be $b = b_{\mathrm{chain}} = 0.2865$ nm, $k_2 = k_{\mathrm{chain}} = 814$ eV/nm^2, and $\phi = \phi_{\mathrm{chain}} = -1.638$ eV. b_{chain} is the DFT equilibrium lattice parameter for infinite Bi chain [see the inset of Fig. 4(a)]. k_{chain} and ϕ_{chain} are estimated from our DFT calculations for the Bi chain. We also take $k_1 = k_{\mathrm{sub}} = 307$ eV/nm^2, which is a typical value estimated from our DFT calculations. Using these parameters (see Supplemental Material, Sec. S3 [44] for estimating all parameters) as input, we obtain the optimized energies per Bi atom, $E = E_{\mathrm{total}}/N$, which are $E_{C0} = 7.982$ eV, $E_{C1} = 9.689$ eV, $E_{C2} = 11.441$ eV, and $E_{C3} = 10.060$ eV for the four shapes, and then $E_{C0} < E_{C1} < E_{C3} < E_{C2}$. Thus, $C0$ is energetically most favorable, while the most compact $C2$ is least favorable. To examine how the results depend on the parameters k_1, k_2, ϕ, and b, we plot E versus the specific parameters r_k, r_ϕ, and b in Fig. S7 [44]. Briefly, the above conclusion remains for varying k_1 and k_2, or ϕ, in reasonable ranges. For b, we find a critical value $b_c \approx 0.4271$ nm (corresponding to a tensile strain $\varepsilon_c \approx 7.27\%$), i.e., $C0$ is more favorable than $C1$ and $C2$ for $b < b_c$ (or $\varepsilon > \varepsilon_c$), and unfavorable relative to $C1$ and $C2$ for $b > b_c$ (or $\varepsilon < \varepsilon_c$). See Sec. S2.3 [44] for details. Therefore, our key finding is that $C0$ affords more efficient strain relief than $C1$ and $C2$ for larger mismatch strain.

To understand the height levels observed in experiments, we perform DFT calculations for freestanding 1- to 4-ML Bi slabs with thicknesses $L = 1$ to 4. We find three phases (energy minima) for $L = 2$, 3, or 4 in the range of lateral lattice parameter b from 0.3 to 0.7 nm versus only one energy minimum for $L = 1$, as shown in Fig. 4. The existence of these local energy minima reflects the competition between van der Waals and covalent interactions with varying lateral and vertical Bi-Bi distances (b and interlayer spacings d_1, d_2, and/or d_3). The most-stable phases for $L = 1$ to 4 have the equilibrium lattice parameters $b_{1\,\mathrm{ML}} = 0.3304$ nm, $b_{2\,\mathrm{ML}} = 0.4309$ nm, $b_{3\,\mathrm{ML}} = 0.3437$ nm, and $b_{4\,\mathrm{ML}} = 0.4425$ nm, respectively.

Based on the DFT surface energies γ (Table S1 [72]), the stability order is $L = 2$, 4, 1, and 3, i.e., even-L slabs are much more stable than odd-L slabs. $\gamma_{L=1} = 4.091$ eV/nm^2 is relatively high, so the compact 1-ML Bi ($C2$) is not observed in STM images. Instead, the more stable 1-ML ST Bi island ($C0$) forms as level S_1 due to inhibited interlayer transport (level S_1 is metastable relative to level 2; see Sec. S3.5 [44]), as analyzed above. Level 2 corresponds to $L = 2$, which is the most-stable thickness due to the lowest $\gamma_{L=2} = 1.654$ eV/nm^2, and therefore this level has a high occurrence rate in STM images. In contrast, level 4 corresponding to $L = 4$ has a very low occurrence rate in STM images (see, e.g., Fig. 1) because $\gamma_{L=4} = 1.885$ eV/nm^2 is slightly higher than $\gamma_{L=2} = 1.654$ eV/nm^2, while $\gamma_{L=3} = 5.961$ eV/nm^2 is much higher so that 3-ML Bi is unobservable. Level B mainly corresponds to even-L Bi islands with $L > 4$. In addition, metastable phases in Fig. 4 are not generally expected to be observed in experiments. For more stability-analysis details of Bi films, see Sec. S3 [44].

Level S_3 has a significantly high occurrence rate. We interpret this level as a 1-ML ST-like Bi film forming on a superstable 2-ML Bi film, where the nominal 1-ML Bi film has a strain $\varepsilon = 30.42\%$ relative to $l = b_{2\,\mathrm{ML}} = 0.4309$ nm. This strain is also sufficiently large to form 1-ML ST Bi islands on a 2-ML Bi film. As listed in Supplemental Material, Table S2 [44], $C0$ (corresponding to level S_3) is always more favorable than the compact island $C2$ (corresponding to 3-ML Bi) as long as k_1 is not too small. Relative to 3-ML film with $l = b_{3\,\mathrm{ML}} = 0.3437$ nm, 1-ML Bi film has a small strain $\varepsilon = 4.03\%$, and then $C0$ is generally more unfavorable than other shapes (see Table S2 [44] again), i.e., forming ST-like structures on 3-ML Bi film is impossible. Relative to 4-ML (∞-ML) film with $l = b_{4\,\mathrm{ML}}(b_{\infty\,\mathrm{ML}}) = 0.4425(0.4546)$ nm, 1-ML Bi film has a large strain $\varepsilon = 33.93\%(37.59\%)$. However, we expect that k_1 would be significantly reduced with increasing $L > 2$ due to the adlayer Bi is far away from the InSb surface (see Sec. 3.4 [44]). Too small k_1 does not favor formation of ST structure but favor $C2$ (see Table S2 [44]) i.e., forming ST-like structures on 4-ML (∞-ML) Bi film would be unlikely. Instead, level B basically reverts to conventional

homoepitaxy, where the solid triangular islands grow with well-known properties [72] (see, e.g., Fig. S5).

Although we do not include InSb substrate in our DFT calculations, it is informative to compare DFT interlayer spacings in Fig. 4 with height levels in Fig. 1. The height difference between level S_1 and 2 is 0.1832 nm, reasonably consistent with $d_1 = 0.1751$ nm of 2-ML film (phase II). The height difference between level S_1 and 4 is about 0.58 nm, reasonably consistent with $d_1 + d_2 + d_3 = 0.6009$ nm of 4-ML film (phase II). The height difference between level S_1 and S_3 is about 0.39 nm, which happens to be close to Bi bulk $d = 0.4091$ nm.

Finally, we examine electronic topological properties of ST films. Our DFT analysis first demonstrates that free-standing 1- and 3-ML Bi films are topologically trivial, while 2- and 4-ML Bi are topologically nontrivial, consistent with previous predictions [35,36]. Then we perform an electronic structure analysis for a 5×5 supercell with one or seven Bi atoms removed from top Bi ML and find that such configurations are topologically trivial. Thus, a ST Bi film observed in our experiments is likely to be topologically trivial and consequently turn off the topology of nontrivial 2- or 4-ML Bi film. For details, see Sec. S3.7.

In summary, we have realized Bi ST structures grown on InSb(111)B surface. This is the first observation of single-element STs self-assembling on a semiconducting surface. Our STM measurements and theoretical analyses suggest that a ST ML as an adlayer can form on a wetting layer or 2-ML Bi film. The formation of ST structures requires a specifically large adlayer-substrate lattice mismatch (with tensile strain), sufficiently strong adlayer-substrate and intra-adlayer elastic stiffnesses, and sufficiently weak intra-adlayer interatomic interactions. Such fractal ST structures, as observed in our experiments, are expected to be able to turn off the electronic topology of Bi films. Such a feature could potentially provide a controllable way to tune the topological property in a quantum-spin-Hall thin film. This could make the system attractive to explore controlled Majorana Fermion formation for realizing topological quantum computing.

C. L., G. W., Y. Y., C. L., H. H., D. G., Y. L., S. W., H. Z., C. L., and J. J. thank the Ministry of Science and Technology of China (Grants No. 2019YFA0308600, No. 2020YFA0309000, No. 2016YFA0301003, and No. 2016YFA0300403), NSFC (Grants No. 11521404, No. 11634009, No. 92065201, No. 11874256, No. 11874258, No. 12074247, No. 11790313, and No. 11861161003), the Strategic Priority Research Program of Chinese Academy of Sciences (Grant No. XDB28000000), and the Science and Technology Commission of Shanghai Municipality (Grants No. 2019SHZDZX01, No. 19JC1412701, and No. 20QA1405100) for partial support. Y. H. was supported by the Materials Sciences and Engineering Division of the U.S. Department of Energy (USDOE) Office of Science Basic Energy Sciences, and the research was performed at the Ames Laboratory operated by Iowa State University under Contract No. DE-AC02-07CH11358. J. W. E. was supported by the NSF Project No. CHE-1507223. Y. Z. and F. L. were supported by the USDOE Office of Science Basic Energy Sciences under Grant No. DE-FG02-04ER46148. DFT calculations were performed with the Extreme Science and Engineering Discovery Environment (XSEDE), which is supported by the National Science Foundation under Grant No. ACI-1548562, and also used resources of the National Energy Research Scientific Computing Center (NERSC), a USDOE Office of Science User Facility operated under Contract No. DE-AC02-05CH11231.

*Corresponding author.
y27h@ameslab.gov
†Corresponding author.
jfjia@sjtu.edu.cn

[1] W. Sierpiński, C. R. Acad. Sci. **160**, 302 (1915), https://gallica.bnf.fr/ark:/12148/bpt6k31131/f302.item.
[2] F. Hausdorff, Math. Ann. **79**, 157 (1918).
[3] E. Conversano and L. T. Lalli, Aplimat J. Appl. Math. **4**, 113 (2011), http://www.aplimat.com/index.php/aplimat-archive/volume-4.
[4] S. Wolfram, Am. Math. Mon. **91**, 566 (1984).
[5] D. G. Poole, Math. Mag. **67**, 323 (1994).
[6] M. F. Barnsley, *Fractals Everywhere*, 2nd ed. (Academic Press, New York, 1993), https://www.elsevier.com/books/fractals-everywhere/barnsley/978-0-12-079061-6.
[7] S. Wolfram, Rev. Mod. Phys. **55**, 601 (1983).
[8] P. W. K. Rothemund, N. Papadakis, and E. Winfree, PLOS Biol. **2**, e424 (2004).
[9] J. I. Lathrop, J. H. Lutz, and S. M. Summers, Theor. Comput. Sci. **410**, 384 (2009).
[10] J. Kou, Y. Liu, F. Wu, J. Fan, H. Lu, and Y. Xu, J. Appl. Phys. **106**, 054905 (2009).
[11] J. A. Fan, W.-H. Yeo, Y. Su, Y. Hattori, W. Lee, S.-Y. Jung, Y. Zhang, Z. Liu, H. Cheng, L. Falgout *et al.*, Nat. Commun. **5**, 3266 (2014).
[12] E. van Veen, S. Yuan, M. I. Katsnelson, M. Polini, and A. Tomadin, Phys. Rev. B **93**, 115428 (2016).
[13] K Wang, Y. Liu, and T. Liang, Physica (Amsterdam) **498B**, 33 (2016).
[14] M. Brzezińska, A. M. Cook, and T. Neupert, Phys. Rev. B **98**, 205116 (2018).
[15] D. F. Nicola, N. S. P. Purayil, D. Spirito, M. Miscuglio, F. Tantussi, A. Tomadin, F. D. Angelis, M. Polini, R. Krahne, and V. Pellegrini, ACS Photonics **5**, 2418 (2018).
[16] Y. Wang, N. Xue, R. Li, T. Wu, N. Li, S. Hou, and Y. Wang, ChemPhysChem **20**, 2262 (2019).
[17] H. Huang and F. Liu, Phys. Rev. Lett. **121**, 126401 (2018).
[18] H. Huang and F. Liu, Phys. Rev. B **98**, 125130 (2018).
[19] S. L. Tait, Nat. Chem. **7**, 370 (2015).
[20] R. Sarkar, K. Guo, C. N. Moorefield, M. J. Saunders, C. Wesdemiotis, and G. R. Newkome, Angew. Chem., Int. Ed. Engl. **53**, 12182 (2014).

[21] J. Shang, Y. Wang, M. Chen, J. Dai, X. Zhou, J. Kuttner, G. Hilt, X. Shao, J. M. Gottfried, and K. Wu, Nat. Chem. **7**, 389 (2015).

[22] X. Zhang, N. Li, L. Liu, G. Gu, C. Li, H. Tang, L. Peng, S. Hou, and Y. Wang, Chem. Commun. **52**, 10578 (2016).

[23] X. Zhang, N. Li, G.-C. Gu, H. Wang, D. Nieckarz, P. Szabelski, Y. He, Y. Wang, C. Xie, Z.-Y. Shen *et al.*, ACS Nano **9**, 11909 (2015).

[24] N. Li, X. Zhang, G.-C. Gu, H. Wang, D. Nieckarz, P. Szabelski, Y. He, Y. Wang, J.-T. Lü, H. Tang *et al.*, Chin. Chem. Lett. **26**, 1198 (2015).

[25] Q. Sun, L. Cai, H. Ma, C. Yuan, and W. Xu, Chem. Commun. **51**, 14164 (2015).

[26] A. Rastgoo-Lahrood, N. Martsinovich, M. Lischka, J. Eichhorn, P. Szabelski, D. Nieckarz, T. Strunskus, K. Das, M. Schmittel, W. M. Heckl, and M. Lackinger, ACS Nano **10**, 10901 (2016).

[27] G. Gu, N. Li, L. Liu, X. Zhang, Q. Wu, D. Nieckarz, P. Szabelski, L. Peng, B. K. Teo, S. Hou *et al.*, RSC Adv. **6**, 66548 (2016).

[28] N. Li, G. Gu, X. Zhang, D. Song, Y. Zhang, B. K. Teo, L. Peng, S. Hou, and Y. Wang, Chem. Commun. **53**, 3469 (2017).

[29] C. Li, X. Zhang, N. Li, Y. Wang, J. Yang, G. Gu, Y. Zhang, S. Hou, L. Peng, K. Wu *et al.*, J. Am. Chem. Soc. **139**, 13749 (2017).

[30] S. N. Kempkes, M. R. Slot, S. E. Freeney, S. J. M. Zevenhuizen, D. Vanmaekelbergh, I. Swart, and C. M. Smith, Nat. Phys. **15**, 127 (2019).

[31] Y. Mo, T. Chen, J. Dai, K. Wu, and D. Wang, J. Am. Chem. Soc. **141**, 11378 (2019).

[32] D. Nieckarz and P. Szabelski, Chem. Commun. **50**, 6843 (2014).

[33] D. Nieckarz and P. Szabelski, Chem. Commun. **52**, 11642 (2016).

[34] S. Murakami, Phys. Rev. Lett. **97**, 236805 (2006).

[35] Z. Liu, C.-X. Liu, Y.-S. Wu, W.-H. Duan, F. Liu, and J. Wu, Phys. Rev. Lett. **107**, 136805 (2011).

[36] Z. F. Wang, L. Chen, and F. Liu, Nano Lett. **14**, 2879 (2014).

[37] F. Yang, L. Miao, Z. F. Wang, M.-Y. Yao, F. Zhu, Y. R. Song, M.-X. Wang, J.-P. Xu, A. V. Fedorov, Z. Sun, G. B. Zhang, and C. Liu, F. Liu, D. Qian, C. L. Gao, and J. F. Jia, Phys. Rev. Lett. **109**, 016801 (2012).

[38] H.-H. Sun, M.-X. Wang, F. Zhu, G.-Y. Wang, H.-Y. Ma, Z.-A. Xu, Q. Liao, Y. Lu, C.-L. Gao, Y.-Y. Li *et al.*, Nano Lett. **17**, 3035 (2017).

[39] M. Zhou, W. Ming, Z. Liu, Z. Wang, P. Li, and F. Liu, Proc. Natl. Acad. Sci. U.S.A. **111**, 14378 (2014).

[40] C.-H. Hsu, Z.-Q. Huang, F.-C. Chuang, C.-C. Kuo, Y.-T. Liu, H. Lin, and A. Bansil, New J. Phys. **17**, 025005 (2015).

[41] P. Li, M. Zhou, L. Zhang, Y. Guo, and F. Liu, Nanotechnology **27**, 095703 (2016).

[42] F. Reis, G. Li, L. Dudy, M. Bauernfeind, S. Glass, W. Hanke, R. Thomale, J. Schäfer, and R. Claessen, Science **357**, 287 (2017).

[43] N. Shimamura, K. Sugawara, S. Sucharitakul, S. Souma, K. Iwaya, K. Nakayama, C. X. Trang, K. Yamauchi, T. Oguchi, K. Kudo *et al.*, ACS Nano **12**, 10977 (2018).

[44] See Supplemental Material at http://link.aps.org/supplemental/10.1103/PhysRevLett.126.176102 for crystalline structures, STM measurement, model details, DFT calculation details, additional data, and additional discussions, which includes Refs. [45–57].

[45] Y. Han, D.-J. Liu, and J. W. Evans, Nano Lett. **14**, 4646 (2014).

[46] W. Li, L. Huang, J. W. Evans, and Y. Han, Phys. Rev. B **93**, 155416 (2016).

[47] W. Li, L. Huang, R. G. S. Pala, G.-H. Lu, F. Liu, J. W. Evans, and Y. Han, Phys. Rev. B **96**, 205409 (2017).

[48] G. Kresse and D. Joubert, Phys. Rev. B **59**, 1758 (1999).

[49] G. Kresse and J. Furthmüller, Phys. Rev. B **54**, 11169 (1996).

[50] J. Klimeš, D. R. Bowler, and A. Michaelides, J. Phys. Condens. Mat. **22**, 022201 (2010).

[51] Y. Han, K. C. Lai, A. Lii-Rosales, M. C. Tringides, J. W. Evans, and P. A. Thiel, Surf. Sci. **685**, 48 (2019).

[52] Y. Han, M. C. Tringides, J. W. Evans, and P. A. Thiel, Phys. Rev. Research **2**, 013182 (2020).

[53] W.-K. Huang, K.-W. Zhang, C.-L. Yang, H. Ding, X. Wan, and S.-C. Li, Nano Lett. **16**, 4454 (2016).

[54] A. A. Mostofi, J. R. Yates, Y.-S. Lee, I. Souza, D. Vanderbilt, and N. Marzari, Comput. Phys. Commun. **178**, 685 (2008).

[55] F. Ersan, E. Aktürk, and S. Ciraci, Phys. Rev. B **94**, 245417 (2016).

[56] W. Li, L. Huang, M. C. Tringides, J. W. Evans, and Y. Han, J. Phys. Chem. Lett. **11**, 9725 (2020).

[57] C. Kittel, *Introduction to Solid State Physics*, 7th ed. (John Wiley & Sons, New York, 1996).

[58] T. Nakada, T. Ikeda, M. Yata, and T. Osaka Surf. Sci. **222**, L825 (1989).

[59] T. Nakada and T. Osaka, Phys. Rev. Lett. **67**, 2834 (1991).

[60] L. Ö. Olsson, J. Kanski, L. Ilver, C. B. M. Andersson, M. Björkqvist, M. Göthelid, U. O. Karlsson, and M. C. Håkansson, Phys. Rev. B **50**, 18172 (1994).

[61] J. Wever, H. L. Meyerheim, W. Moritz, V. Jahns, D. Wolf, H. Schulz, L. Seehofer, and R. L. Johnson, Surf. Sci. **321**, L225 (1994).

[62] M. Björkqvist, M. Göthelid, L. Ö. Olsson, J. Kanski, and U. O. Karlsson, J. Vac. Sci. Technol. B **14**, 957 (1996).

[63] S. Cho, Y.-H. Um, Y. Kim, G. K. L. Wong, J. B. Ketterson, and J.-I. Hong, J. Vac. Sci. Technol. A **20**, 1191 (2002).

[64] K. Inada, R. Takahashi, N. Naruse, T. Kadohira, S.-P. Cho, and T. Osaka, J. Surf. Sci. Soc. Jpn. **24**, 105 (2003).

[65] J. Mäkelä, Z. S. J. Rad, J.-P. Lehtiö, M. Kuzmin, M. P. J. Punkkinen, P. Laukkanen, and K. Kokko, Sci. Rep. **8**, 14382 (2018).

[66] P. Cucka and C. S. Barrett, Acta Cryst. **15**, 865 (1962).

[67] D. Schiferl and C. S. Barrett, J. Appl. Crystallogr. **2**, 30 (1969).

[68] I. Vurgaftman, J. R. Meyer, and L. R. Ram-Mohan, J. Appl. Phys. **89**, 5815 (2001).

[69] J. Tersoff and F. K. LeGoues, Phys. Rev. Lett. **72**, 3570 (1994).

[70] F. Liu and M. G. Lagally, Surf. Sci. **386**, 169 (1997).

[71] B. D. Krack, V. Ozoliņš, M. Asta, and I. Daruka, Phys. Rev. Lett. **88**, 186101 (2002).

[72] T. Michely and J. Krug, Islands, Mounds and Atoms, Springer Series in Surface Sciences Vol. **42**, https://link.springer.com/book/10.1007/978-3-642-18672-1.

Supplemental Material

Sierpiński Thin Film Structure Turning off the Electronic Topology in Bi Films on InSb(111)B Surfaces

Chen Liu,[1] Yinong Zhou,[2] Guanyong Wang,[3] Yin Yin,[1] Can Li,[1] Haili Huang,[1] Dandan Guan,[1,4] Yaoyi Li,[1,4] Shiyong Wang,[1,4] Hao Zheng,[1,4] Canhua Liu,[1,4] Yong Han,[5,6,*] James W. Evans,[5,6] Feng Liu,[2] and Jinfeng Jia[1,4†]

[1]*Key Laboratory of Artificial Structures and Quantum Control (Ministry of Education), Shenyang National Laboratory for Materials Science, School of Physics and Astronomy, Shanghai Jiao Tong University, Shanghai 200240, China.*
[2]*Department of Materials Science and Engineering, University of Utah, Salt Lake City, Utah 84112, USA*
[3]*Shenzhen Institute for Quantum Science and Engineering, Southern University of Science and Technology, Shenzhen 518055, China*
[4]*Tsung-Dao Lee Institute, Shanghai Jiao Tong University, Shanghai 200240, China*
[5]*Department of Physics and Astronomy, Iowa State University, Ames, Iowa 50011, USA*
[6]*Ames Laboratory, U. S. Department of Energy, Ames, Iowa 50011, USA*

*Corresponding author:
y27h@ameslab.gov
†Corresponding author:
jfjia@sjtu.edu.cn

Contents

S0. Crystalline structures of bulk Bi and InSb

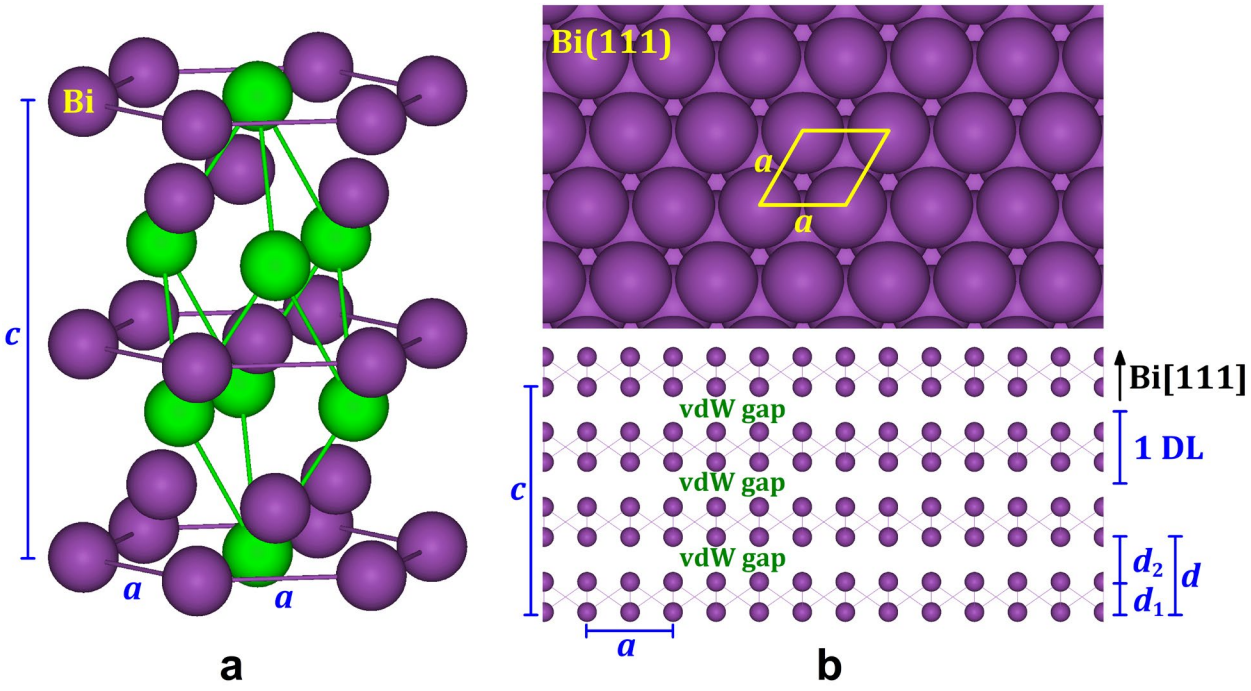

FIG. S1. The α-As structure of Bi bulk crystal. **(a)** A hexagonal cell of α-As structure of bulk Bi crystal with the lattice constants a and c. The green atoms define a rhombohedral primitive cell. **(b)** Upper panel: Top view of a truncated bulk Bi(111) surface. A lateral 1×1 unit cell with the lattice constant a is indicated. Lower panel: Side view of the Bi(111) slab. Lattice constants (a and c), interlayer spacings (d_1, d_2, and $d = d_1 + d_2$), and the vdW-like gaps are indicated. One Bi double layer (DL) consists of two adjacent covalent-bonded Bi monatomic layers (MLs), i.e., 1 DL = 2 MLs (which is sometimes called "1 bilayer" in previous literature; also see the definition of ML in Sec. S1). For α-As structure of bulk Bi, the experimental lattice parameters at 298 K [66,67] are: $a = 0.4546$ nm, $c = 1.1862$ nm, and $u = 0.23389$. Correspondingly, the interlayer spacings along Bi[111] direction are $d_1 = (2u - 1/3)c = 0.1595$ nm, $d_2 = (2/3 - 2u)c = 0.2359$ nm, and $d = d_1 + d_2 = c/3 = 0.3954$ nm.

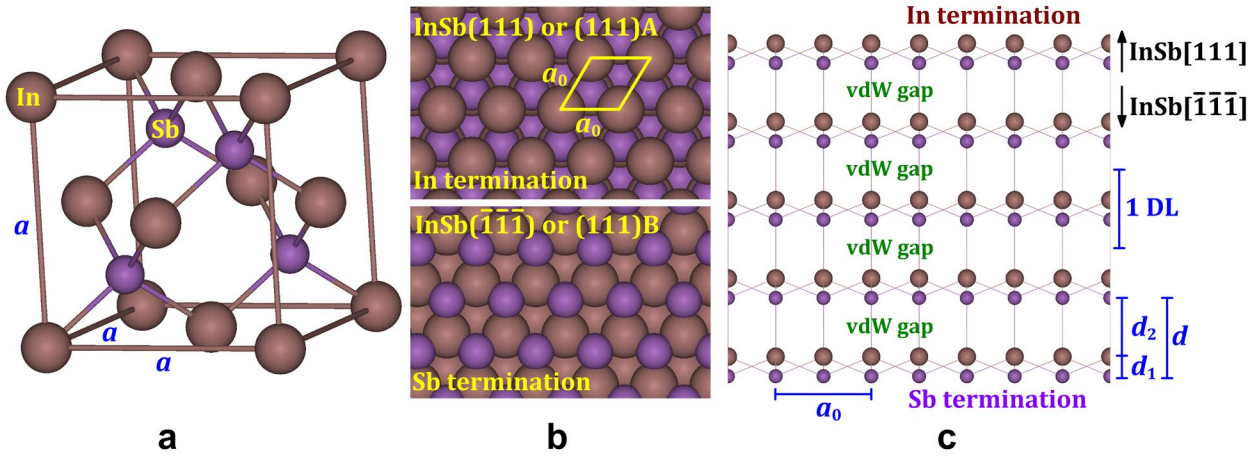

FIG. S2. The zincblende structure of InSb bulk crystal. **(a)** A cubic unit cell of zincblende structure of bulk InSb crystal. **(b)** Upper panel: Top view of a truncated bulk InSb(111) surface with In termination, which is often called InSb(111)A surface. A lateral 1×1 unit cell with the lateral lattice constant $a_0 = a/\sqrt{2}$ is indicated. Lower panel: Top view of a truncated bulk InSb($\bar{1}\bar{1}\bar{1}$) surface with Sb termination, which is often called InSb(111)B surface. **(c)** Side view of the InSb(111) slab. Lateral lattice constant (a_0), interlayer spacings (d_1, d_2, and $d = d_1 + d_2$), vdW-like gaps, crystalline orientations, and surface terminations are indicated. One In-Sb DL consists of 1-ML In and 1-ML Sb. For zincblende structure of bulk InSb, the experimental lattice parameter at 298 K is $a = 0.64794$ nm [68]. Correspondingly, the (111) surface lattice constant $a_0 = a/\sqrt{2} = 0.45816$ nm, the interlayer spacings are $d_1 = a\sqrt{3}/12 = 0.09352$ nm, $d_2 = a\sqrt{3}/4 = 0.28057$ nm, and $d = a/\sqrt{3} = d_1 + d_2 = 0.37409$ nm.

S1. STM measurement

All experiments were carried out with a commercial UHV molecular-beam-epitaxy STM system at a base pressure less than 1×10^{-10} Torr. The InSb(111) substrates were cleaned by about 3 cycles of Ar^+ ion sputtering and annealing about 0.5 h at about 673 K. High-purity Bi (99.999%) was evaporated and deposited on InSb(111)B substrate surface by a deposition rate of about 0.003 ML/s at a deposition temperature T_{dep}. The range of T_{dep} in the experiments of this work is about 348 K to 453 K. For all experiments (unless otherwise specified), after the deposition up to a required Bi coverage θ (in unit of ML) on the InSb(111)B substrate surface, the system was cooled down by a time t_{cool} to room temperature (RT) and followed by about 1 h under RT, and then put into an environment at the liquid helium temperature of about 4 K, where the STM measurement was carried out with a chemically etched tungsten tip. The time from putting the system into the environment of the liquid helium temperature to STM measurement was about 1.5 h to 2 h. Here, it should be mentioned that we also performed the STM measurements in an environment at the liquid nitrogen temperature of about 77 K, and found the similar Bi morphologies on InSb(111)B substrate surface (not shown) to those measured in the above environment at the liquid helium temperature of about 4 K.

From the STM images observed at different Bi coverages (e.g., see Figs. S4–S6), the growth mode of Bi is layer-by-layer-like, and thus we use monatomic layers (MLs) as the unit of the coverage θ, where 1 ML means that all lattice sites in one Bi(111) monatomic layer (see Fig. S1) are occupied by Bi atoms. Also note that a conventional buckled layer in a Bi(111) or InSb(111) slab is of 2 ML, i.e., one double layer (1 DL) (see Figs. S1–S2).

To determine the deposition rate or flux F and the coverage $\theta = Ft$ at the deposition time t, we first obtain the oscillation period of the RHEED intensity for Bi depositing on a Si(111)-(7×7) surface as a benchmark. During deposition for any higher coverage θ, the oscillation period reaches a constant value and corresponds to $\theta = 1$ DL or 2 ML of Bi(111) film with a Bi bulk lattice parameter a. On the other hand, we also check the corresponding STM images to ensure the perfect consistency of the coverage measured from the two approaches. The determined F is about 0.003 ML/s. Then, we always use this flux for Bi deposition on InSb(111)B substrate and the coverage is obtained always by $\theta = Ft$.

Here, we provide more experimental parameters in Figs. 1 and 2. For all STM images in Figs. 1 and 2, $T_{\mathrm{dep}} \approx 423$ K and $t_{\mathrm{cool}} \approx 1$ h. In Fig. 1a, STM image size is 100 nm × 100 nm, Bi coverage $\theta \approx 2$ ML, $I = 100$ pA, and $V = +1.60$ V. In Fig. 1b, STM image size is 100 nm × 100 nm, Bi coverage $\theta \approx 2$ ML, $I = 100$ pA, and $V = +2.00$ V. In Fig. 2a, STM image size is 30 nm × 30 nm, Bi coverage $\theta \approx 1$ ML, $I = 100$ pA, and $V = +2.50$ V.

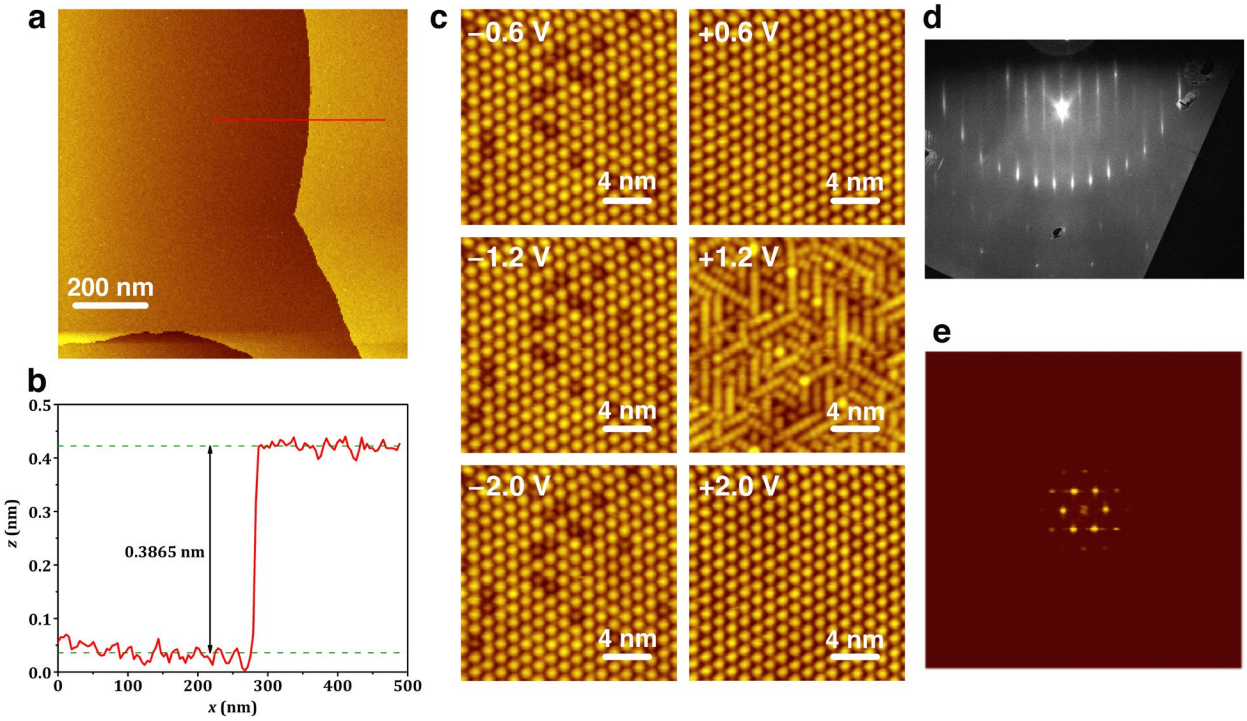

FIG. S3. Clean InSb(111)B substrate. **(a)** A large-scale STM image (size: 1000 nm × 1000 nm) for morphology of InSb(111)B surface with steps; $I = 100$ pA and $V = +2.07$ V. **(b)** Height line profile for a step in (a). The step height of about 0.3865 nm indicates a good agreement with the previous experimental value of bulk InSb(111) DL thickness $d = 0.37409$ nm (Fig. S2). **(c)** Atomically resolved STM images for the same region (size: 20 nm × 20 nm) of the InSb(111)B surface under different bias with $I = 100$ pA. **(d)** RHEED pattern of InSb(111)B, indicating a (3×3) reconstruction. **(e)** 2D-FFT image of InSb(111)B for the image of +2.0 V in (c). From (e), the in-plane lattice constant is estimated as about 1.4 nm, which is approximately equal to $3a_0 = 1.37448$ nm (see Fig. S2 for a_0) and therefore also indicates a (3×3) reconstruction of the InSb(111)B surface. All STM images were measured at the liquid nitrogen temperature of about 77 K. The STM results in (c) are generally consistent with previous experimental observations [60,61,64,65], although STM images with sufficiently-high resolution to identify the exact atomic positions in the reconstructed surface are still unavailable.

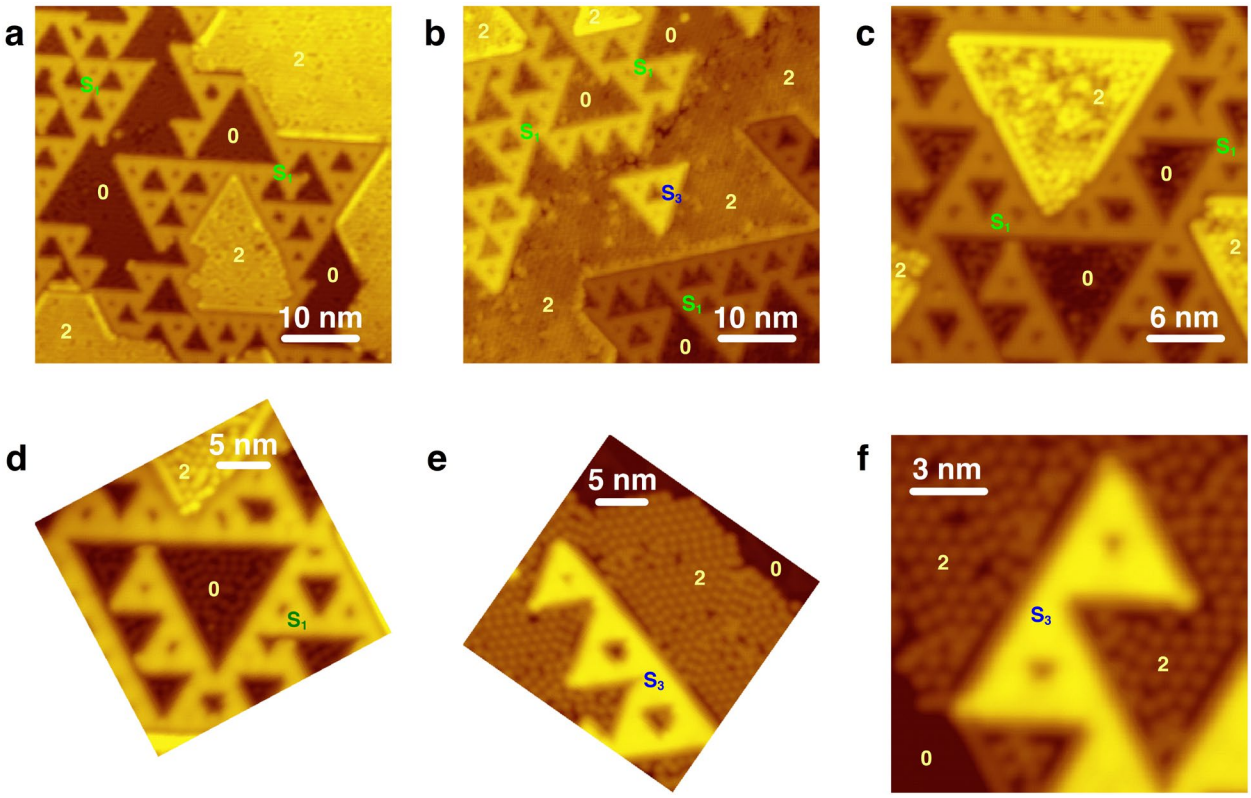

FIG. S4. STM images showing the surface morphologies with the ST-like Bi islands grown on InSb(111)B surface for different surface regions. Island height levels are labelled (see the main text for explanation). **(a)** Image size: 50 nm × 50 nm; $I = 100$ pA and $V = +1.10$ V; coverage: $\theta \approx 1$ ML. **(b)** Image size: 50 nm × 50 nm; coverage: $\theta \approx 1$ ML; $I = 100$ pA and $V = +1.01$ V. Note that there is an InSb step along the diagonal direction from lower left to upper right in this image. **(c)** Image size: 30 nm × 30 nm; coverage: $\theta \approx 2$ ML; $I = 100$ pA, $V = +1.10$ V. **(d)** Image size: 28 nm × 28 nm; coverage: $\theta \approx 2$ ML; $I = 100$ pA and $V = +1.00$ V. **(e)** Image size: 28 nm × 28 nm; coverage: $\theta \approx 1$ ML; $I = 100$ pA and $V = +1.02$ V. **(f)** Image size: 15 nm × 15 nm; coverage: $\theta \approx 2$ ML; $I = 100$ pA and $V = +1.00$ V. For all these STM images, $T_{\mathrm{dep}} \approx 423$ K, and $t_{\mathrm{cool}} \approx 1$ h (see Sec. S1 for explanations).

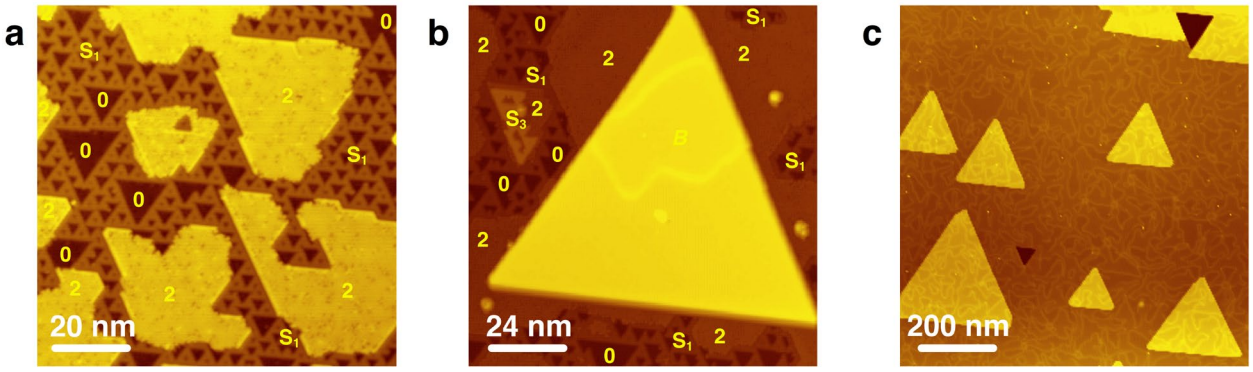

FIG. S5. STM images showing the surface morphologies with Bi islands grown on InSb(111)B surface for different coverages. Island height levels are labelled (see the main text for explanation). **(a)** Coverage: $\theta \approx 1$ ML; image size: 100 nm × 100 nm ($I = 100$ pA, $V = +2.07$ V). **(b)** Coverage: $\theta \approx 2$ ML; image size: 120 nm × 120 nm ($I = 100$ pA, $V = +1.50$ V). **(c)** Coverage: $\theta \approx 5$ ML; image size: 1000 nm × 1000 nm ($I = 100$ pA, $V = +2.07$ V). For all these STM images, $T_{\mathrm{dep}} \approx 403$ K and $t_{\mathrm{cool}} \approx 1$ h (see Sec. S1 for explanations).

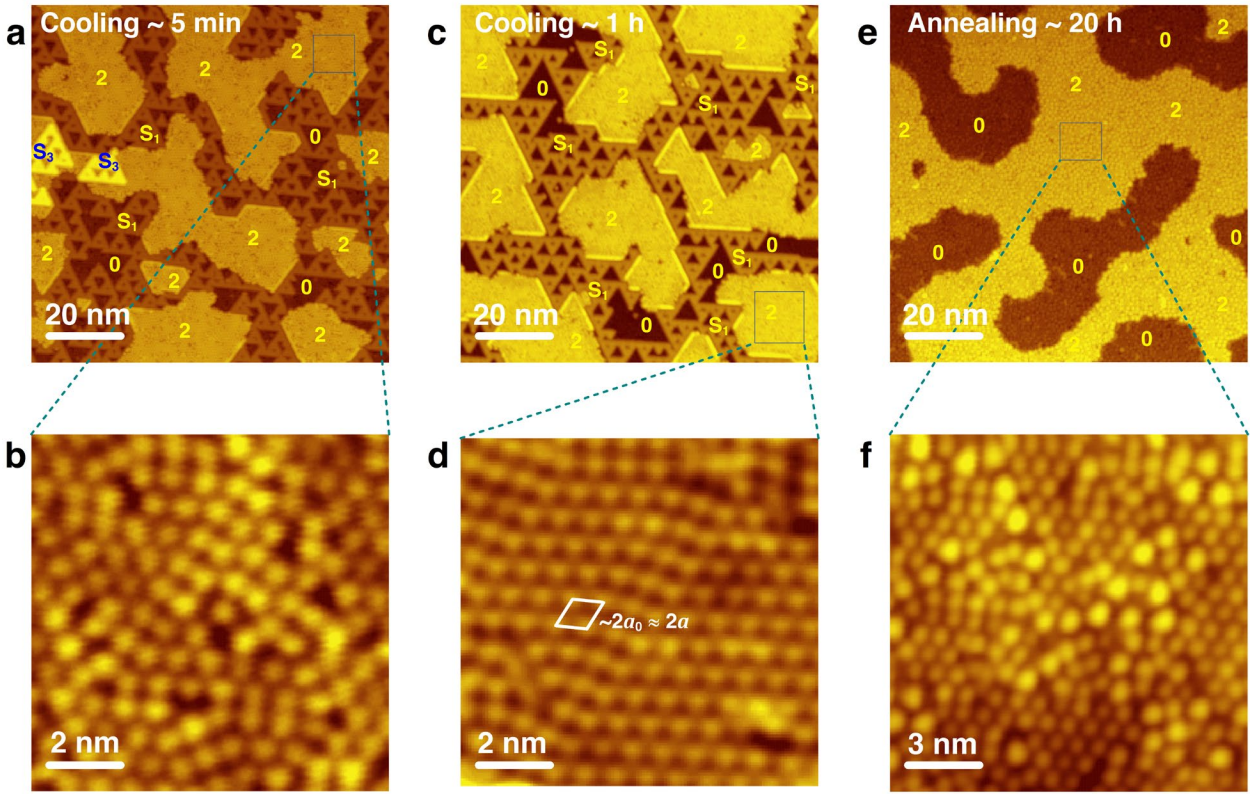

FIG. S6. STM images showing the surface morphologies with Bi islands on InSb(111)B surface for different time controls. Island height levels are labelled (see the main text for explanation). **(a)** $T_{\mathrm{dep}} \approx 403$ K and $t_{\mathrm{cool}} \approx 5$ min; image size: 100 nm × 100 nm; coverage: $\theta \approx 1$ ML; $I = 100$ pA and $V = +1.43$ V. **(b)** Enlargement for the framed region in (a) shows a disordered surface. Image size: 10 nm × 10 nm; $I = 100$ pA and $V = +0.50$ V. **(c)** $T_{\mathrm{dep}} \approx 403$ K and $t_{\mathrm{cool}} \approx 1$ h; image size: 100 nm × 100 nm; coverage: $\theta \approx 1$ ML; $I = 100$ pA and $V = +1.68$ V. **(d)** Enlargement for the framed region in (c) reveals a (2×2)-reconstructed-like surface, as indicated by a rhombus with the measured side length of about $2a_0$ or $2a$, where $a_0 \approx a$ is the lattice constant of InSb(111) plane and a is the lattice constant of Bi(111) plane. Image size: 10 nm × 10 nm; $I = 100$ pA and $V = +0.50$ V. **(e)** After the measurement for (a), the temperature was elevated to RT within about 2 h, and then to 403 K within about 1 h. After that, 403 K was kept for about 20 h. Then, the temperature was cooled down back to RT within about 1 h and the image was measured at liquid helium temperature as in the procedure for measurements of other STM images; image size: 100 nm × 100 nm; coverage: $\theta \approx 1$ ML; $I = 100$ pA and $V = +1.68$ V. **(f)** Enlargement for the framed region in (e) shows a disordered surface. Image size: 15 nm × 15 nm; $I = 100$ pA and $V = +0.50$ V.

S2. Model details

S2.1. Energy formulation

For a 1-ML Bi island with N Bi atoms adsorbed on a substrate surface at specific lattice sites with a lattice constant l, the total energy can be expressed as

$$E_{\text{total}} = E_{\text{electronic}} + E_{\text{elastic}}^{\text{Bi-sub}} + E_{\text{elastic}}^{\text{Bi-Bi}}, \tag{1}$$

based on a generic form of Frenkel-Kontrova-type Hamiltonian for elastic relaxations in bulk alloys [71].

The first term $E_{\text{electronic}}$ in Eq. (1) is the contribution from all electronic effects not associated with relaxations. This term includes various many-body (pair, trio, quarto, …) interactions. For a most simplified model, here we can define an "effective" pair interaction ϕ_i by letting

$$E_{\text{electronic}} = \sum_{i=1}^{M} \phi_i \approx M\phi, \tag{2}$$

where the total contribution $E_{\text{electronic}}$ is decomposed into M "quasi-pair (QP)" interactions between two NN atoms and M is the total number of QPs of the island. The QP interaction ϕ_i generally satisfies $\phi_i < 0$, i.e., the atoms aggregate by attraction. In principle, the QP interaction ϕ_i for the ith atom can be obtained by solving the linear equations corresponding to the various configurations with many-body interactions (e.g., see Refs. 45–47) and generally different from those for other atoms, depending its surrounding (e.g., its NN number), but we take all ϕ_i to be approximately equal to a single parameter ϕ for a specific configuration in our analysis for this work.

Assume that any lattice point of the substrate surface is the equilibrium site of a single Bi atom adsorbed on the substrate surface. The second term $E_{\text{elastic}}^{\text{Bi-sub}}$ in Eq. (1) describes the elastic contribution of Bi atoms away from the equilibrium sites (i.e., the lattice points of the substrate surface) for the Bi island. If we assume that each Bi atom is in a harmonic potential well for this elastic effect, then this term can be expressed as

$$E_{\text{elastic}}^{\text{Bi-sub}} = \frac{1}{2}\sum_{i=1}^{N}\left[k_{ix}(x_i - x_{0i})^2 + k_{iy}(y_i - y_{0i})^2\right] \tag{3}$$

under the Cartesian coordinates, where x_i and y_i are the position coordinates of the ith Bi atom with its corresponding lattice point fixed at x_{0i} and y_{0i}; the elastic tensors k_{ix} and k_{iy} characterize the stiffnesses of the coupling between the ith Bi atom and its lattice point along x and y directions and are therefore related to the property of the substrate. Generally, the values of these elastic tensors vary depending on the position of each Bi atom. For simplicity, in this work we treat all of them as an adlayer-substrate spring parameter $k_1 \approx k_{ix} \approx k_{iy}$ for $i = 1, 2, \ldots, N$.

The third term $E_{\text{elastic}}^{\text{Bi-Bi}}$ in Eq. (1) describes the total elastic energy of all Bi atoms away from their equilibrium lattice sites for a Bi island *without the substrate*. We assume that

only NN Bi pairs have the elastic contributions, and each pair is simplified as a harmonic oscillator. Then, this term can be expressed as

$$E_{\text{elastic}}^{\text{Bi-Bi}} = \frac{1}{2}\sum_{i=1}^{N}\sum_{j_i=1}^{n_i} k_{j_i}\left[\sqrt{\left(x_i - x_{j_i}\right)^2 + \left(y_i - y_{j_i}\right)^2} - b_{ij_i}\right]^2, \quad (4)$$

where n_i is the number of NN pairs of the ith atom after subtracting repeated NN pairs from other atoms (i.e., the sum for n_i is over all NN pairs); the coordinates of the j_ith NN atom of the ith atom are x_{j_i} and y_{j_i}; the elastic tensor k_{j_i} characterizes the stiffness of the coupling between two Bi atoms of each NN pair along the pair bonding direction (again, the value of the elastic tensor generally varies depending on the position of each Bi pair and, for simplicity, in this work we treat any of them as an intra-adlayer spring parameter $k_2 \approx k_{j_i}$ for $i = 1, 2, \ldots, N$ and $j_i = 1, 2, \ldots, n_i$); b_{ij_i} denotes the equilibrium lattice distance between the ith atom and its j_ith NN atom. For an infinite island (i.e., a complete ML), $b_{ij_i} = b$, where b is the lateral lattice constant of the complete ML. For finite Bi islands in this work, we assume $b_{ij_i} \approx b$, but treat b as a parameter which depends on the configurations of the islands that we consider.

To analyze the thermodynamic stabilities of Bi islands with the same number of Bi atoms, N, one can construct a series of specific shapes made up of the N Bi atoms, and then compare the total energies after minimizing Eq. (1) by appropriately choosing the parameters l, ϕ, b, k_1, and k_2. The choices of these parameters reflect the geometric and mechanical properties of structures observed under the experimental conditions. We take these parameters referring to relevant experimental information and our DFT results. For our DFT calculation details of estimating these parameters, see below.

S2.2. Algorithm for energy minimization for our model

We use the conjugate gradient method to execute the energy minimization in the above proposed model.

S2.3. Parameter dependences of energy

Let us first look at k_1 and k_2. From Eqs. (1) to (4), it is obvious that increasing (decreasing) k_1 or/and k_2 will increase (decrease) the contributions from elastic effects. As a benchmark analysis, if k_1 or (and) k_2 is (are) taken to be zero, then the optimized energy will be determined by only Eq. (2), i.e., the energy order of the configurations is trivially determined by the parameter ϕ and the number M of QPs. In this case, if we take the above ϕ values estimated from our DFT calculations, then we obtain $E_{\text{C0}} = -1.872$ eV, $E_{\text{C1}} = -2.006$ eV, $E_{\text{C2}} = -2.079$ eV, and $E_{\text{C3}} = -1.656$ eV, i.e., $E_{\text{C2}} < E_{\text{C1}} < E_{\text{C0}} < E_{\text{C3}}$. The most compact shape C2 has the lowest energy (i.e., most favorable) due to the largest QP number $M = 743$ and the chain-like shape C3 has the highest energy (i.e., most unstable) due to the smallest $M = 270$ even though ϕ_{chain} is significantly lower than ϕ_{1ML}, while the ST shape C0 is also unstable because of its higher energy. For C0 and C1, the QP number M are 669 and 717, respectively.

Then we switch to other values of k_1 and k_2. In principle, one can separately take k_1 and k_2 for different configurations, but the corresponding comparison can be complex. To give a clearer picture, here we only focus on a special case, in which we simply let $r_k = k_1/k_{\text{sub}} = k_2/k_{1\text{ML}}$ (for C0, C1, and C2) $= k_2/k_{\text{chain}}$ (for C3) (for k_{sub}, see Sec. S3.4). We plot the energies versus the single parameter r_k in Fig. S7a. For any $r_k > 0.073$, the green line is always lowest, indicating the ST shape C0 is always most favorable even though the value of r_k is far from the $r_k = 1$ case already discussed in Fig. 3. For any $r_k > 0.234$, the blue line is always highest, indicating the compact shape C2 is always most unfavorable. For any $0 \leq r_k < 0.040$, the blue line becomes lowest, and the energy order of four configurations is the same as the above trivial case of $k_1 = 0$ and/or $k_2 = 0$. Therefore, from this analysis for varying k_1 and k_2, we can say that the ST shape is always favorable as long as the r_k value is not too small, i.e., forming the ST structure requires larger k_1 and k_2.

Next, we analyze the results for varying ϕ. Again, one can in principle separately vary ϕ values for different configurations, but we here only show a simple special case, in which we let $r_\phi = \phi/\phi_{1\text{ML}}$ (for C0, C1, and C2) $= \phi/\phi_{\text{chain}}$ (for C3). We plot the energies versus the single parameter r_ϕ in Fig. S7b. For any $0 < r_\phi < 13.72$, the green line is always lowest, indicating the ST shape C0 is always most favorable, including the $r_\phi = 1$ case already discussed in Fig. 3. For any $r_\phi > 13.72$, the blue line is always lowest, indicating the compact shape C2 is always most unfavorable, but such a range of too large r_ϕ is generally unphysical. Therefore, from this analysis for varying ϕ, we can say that the ST shape is always favorable as long as the ϕ value is not too large, i.e., forming the ST structure requires the weaker interactions which correspond to a higher $\phi < 0$.

To analyze the results for the energy as a function of Bi ML lattice parameter b, we define the lattice mismatch quantified by the strain

$$\varepsilon = \frac{l - b}{b} \times 100\%, \tag{5}$$

where l is the surface lattice parameter of the substrate. Thus, $\varepsilon > 0$ indicates a tensile strain exerted by the substrate lattice on the Bi ML, while $\varepsilon < 0$ indicates a compressive strain. As shown in Fig. 4, the b value of a Bi ML or a Bi chain at its equilibrium structure is smaller than the b values of most-stable phases for 2-, 3-, and 4-ML Bi films (whose metastable phases with significantly higher energies are not assumed to appear in the experiments of this work), and therefore we only consider the tensile strain in this work. Below, as an example, we take l to be $a_0 = 0.45816$ nm and perform the energy minimization for the b values less than a_0 and make a plot in Fig. S7c.

From Fig. S7c, one can immediately see that the green (E_{C0}) curve is always below the red (E_{C1}) and blue (E_{C2}) curves as long as $b \lesssim 0.4271$ nm (corresponding to the strain of $\varepsilon \gtrsim 7.27\%$), i.e., the ST shape C0 is more favorable than compact shapes (C1 and C2) if one takes the same b value (or takes the slightly different b values) for these shapes. When $b \gtrsim 0.4271$ nm (corresponding to the strain of $\varepsilon \lesssim 7.27\%$), the blue ($E_{\text{C2}}$) curve becomes lowest with increasing b (i.e., decreasing ε), while the green (E_{C0}) curve is gradually elevated lying above the blue and red curves (see the inset in Fig. S7c). This implies that there is a critical b value at $b_{\text{c}} \approx 0.4271$ nm (or equivalently a critical strain value at $\varepsilon_{\text{c}} \approx 7.27\%$). In other words, for a 1-ML Bi island with $b < b_{\text{c}}$ (or equivalently $\varepsilon > \varepsilon_{\text{c}}$), the ST shape C0 is more

favorable than more compact islands C1 and C2, and if $b > b_c$ (or equivalently $\varepsilon < \varepsilon_c$), C0 is unfavorable relative to C1 and C2, i.e., forming the ST structure requires a larger tensile strain $\varepsilon > 0$.

In Fig. S7c, the brown (E_{C3}) curve being below the green curve for $b \lesssim 0.4271$ nm does not mean that C3 must be more favorable than C0, because the value of $b \approx b_{\text{chain}} = 0.2865$ nm for the chain-like shape C3 is significantly smaller than $b \approx b_{1\text{ML}} = 0.3304$ nm for the ST shape C0. The significantly higher strain of 59.92% for a chain than 38.67% for a 1-ML Bi results in an energy difference of $\Delta E_{03} = 2.078$ eV > 0, as shown in Fig. S7c. Therefore, C0 is much more favorable than C3.

Specifically, we also analyze the results for varying lattice parameter l as well as for varying k_1. In Table S2, we listed the model results for a nominal 1-ML Bi film on the substrates with the lattice parameters: $l = a_0 = 0.45816$ nm, $l = b_{2\text{ML}} = 0.4309$ nm, $l = b_{3\text{ML}} = 0.3437$ nm, $l = b_{4\text{ML}} = 0.4425$ nm, and $l = b_{\infty\text{ML}} = 0.4546$ nm, for three typical k_1 values: 10, 307, and 500 eV/nm^2, within the range estimated from the Debye model analysis for single-element materials in Sec. S3.4. $b_{2\text{ML}}$, $b_{3\text{ML}}$, $b_{4\text{ML}}$ and $b_{\infty\text{ML}}$ are the DFT lateral equilibrium lattice parameters of most-stable phases for freestanding 2-, 3-, 4-, and ∞-ML Bi films, respectively (see Fig. 4 and Sec. S3.2). The data (especially see the favorability orders of C0, C1, C2, and C3 for varying l and k_1) listed in Table S2 together with the above analyses for other parameter dependence (Fig. S7) provide strong support for our model analyses and conclusion.

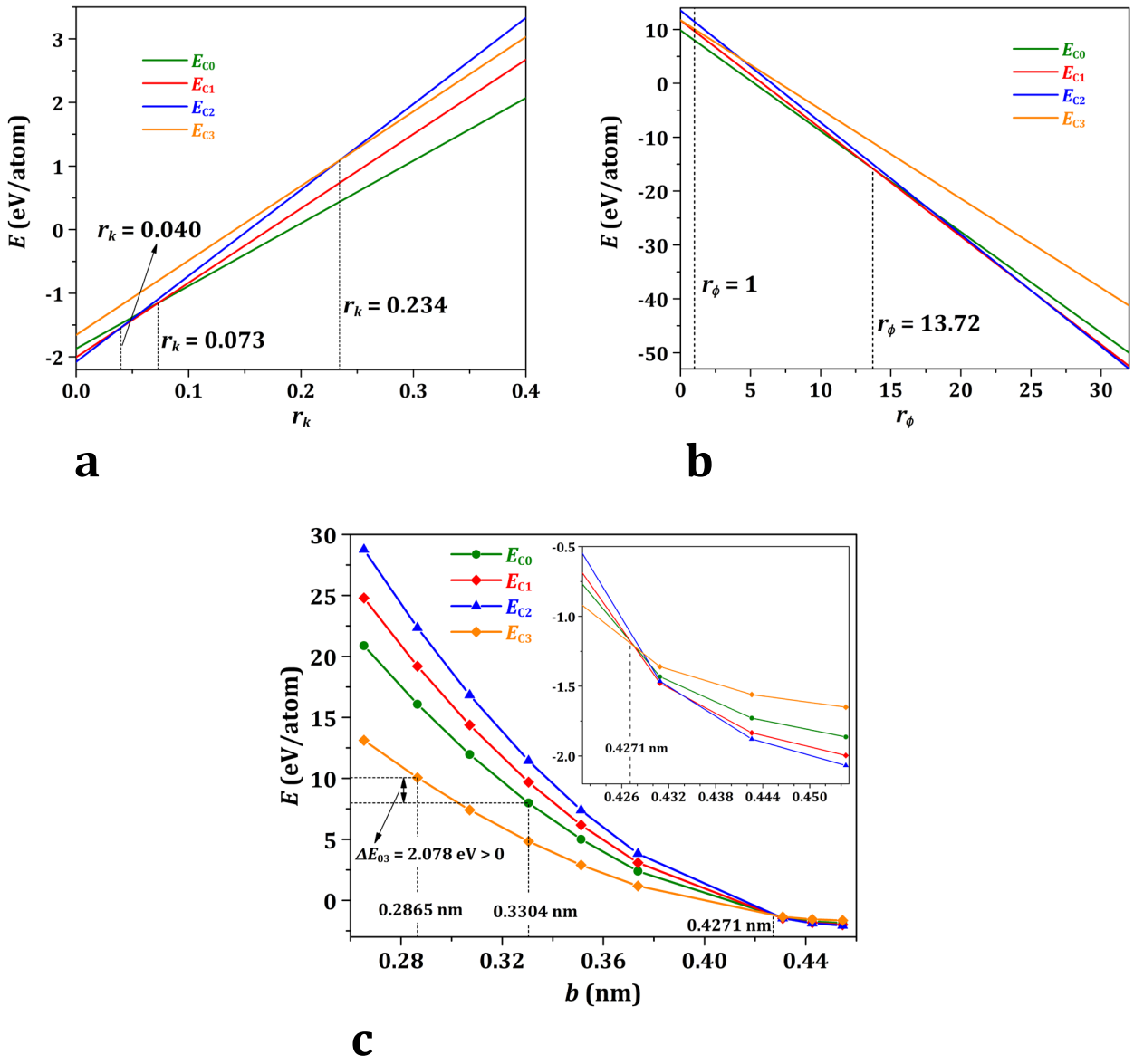

FIG. S7. The optimized energies $E = E_{C0}$, E_{C1}, E_{C2}, and E_{C3} per Bi atom versus various model parameters for four typical configurations (C0, C1, C2, and C3) of 1-ML Bi islands with $N = 267$ Bi atoms after energy minimization. **(a)** E versus r_k. Except k_1 and k_2, the parameters are the same as those listed in the caption of Fig. 3. The vertical dashed lines indicate the intersections of two differently colored solid lines. **(b)** E versus r_ϕ. Except ϕ, the parameters are the same as those listed in the caption of Fig. 3. The vertical dashed lines indicate the intersections of two differently colored solid lines. **(c)** E versus b. The inset is the enlargement for large b values. Other parameters are the same as those listed in the caption of Fig. 3. ΔE_{03} is the energy difference of C0 at $b = b_{1ML} = 0.3304$ nm and C3 at $b = b_{chain} = 0.2865$ nm. For definitions of all parameters, see Sec. S2.1.

S3. DFT method and calculation details

We perform first-principles DFT calculations with the projector-augmented-wave pseudopotentials [48] developed by the Vienna Ab Initio Simulation Package (VASP) [49] group. In the calculations for model parameters and slab energies, we use the optB88-vdW functional [50], where the vdW interactions are included. This functional has already reliably applied for various other systems, e.g., metal plus vdW materials [51,52]. The energy cutoff is taken to be 500 eV. The k mesh is chosen depending on the supercell size for each calculated system. Total energy convergence is reached if the force on any relaxed atom is less than 0.1 eV/nm (for more accurate lattice constant calculations, the tolerance is taken to be less than 0.02 eV/nm). At the free ends of a supercell for modeling a Bi film or a Bi chain, the vacuum thickness between two adjacent replicas is 3 nm. Spin polarization are considered in all calculations. Spin-orbital coupling (SOC) effects are generally insignificant for energy differences of configurations [53], and therefore are not considered. However, we include SOC in the DFT analysis for topological properties of Bi films. We use the wannier90 code [54] to calculate the maximally localized Wannier functions of Bi by fitting the DFT band structures.

S3.1. Bulk properties of Bi

Using the above described DFT method, we obtain the lattice parameters of bulk Bi crystal with an α-As structure (see Fig. S1): $a = 0.4580$ nm, $c = 1.2057$ nm, and $u = 0.23467$, which are in good agreement with the experimental values: $a = 0.4546$ nm, $c = 1.1862$ nm, and $u = 0.23389$ [66,67]. The NN distance is 0.3112 nm from our DFT calculation and the corresponding experimental value is 0.30712 nm. The cohesive energy from our DFT calculations is $E_{\mathrm{c}} = E_{\mathrm{Bi}} - E_{\mathrm{cell}}/n = 3.014$ eV, where E_{cell} is the DFT total energy of the supercell containing n Bi atoms and E_{Bi} is the energy of one Bi atom in gas phase. The E_{c} value of 3.014 eV is consistent with the values of 3.12 eV [55] and 2.988 eV [56] from previous DFT calculations and comparable with the experimental value of 2.18 eV [57]. Other parameters are listed in Table S1. In this DFT calculation, we use a hexagonal unit cell containing six Bi atoms and the k mesh is taken to be $41 \times 41 \times 13$.

S3.2. Phases and equilibrium lattice parameters of chain, 1-, 2-, 3-, and 4-ML Bi

To search the equilibrium lattice parameters of 1-, 2-, 3-, and 4-ML freestanding Bi films as well as freestanding infinite Bi chain, we performed the DFT calculations for total energies versus lattice parameter b. The corresponding results for chemical potential μ are shown in Fig. 4, where μ is defined as $\mu = E_{\mathrm{cell}}/n - E_{\mathrm{Bi}}$ (also see the caption of Table S1).

For 1-ML Bi film (see Fig. 4a), we find one energy minimum at $b = 0.3304$ nm. For $b \lesssim 0.39$ nm, 1-ML Bi film is nonmagnetic. From $b \approx 0.39$ to 5.2 nm, the magnetic moment m increases with increasing b. For $b \gtrsim 5.2$ nm, m values trivially become $3\mu_B$, i.e., the m value for Bi gas phase, as the system approaches to the gas phase and the chemical potential μ approaches to zero. The similar behavior is found for Bi chain, as plotted in the inset of Fig. 4a. One energy minimum for Bi chain is found at $b = 0.2865$ nm, which is slightly larger than the isolated Bi dimer bond length of 0.2654 nm, as listed in Table S1.

For 2-ML Bi film (see Fig. 4b), we find three energy minima at $b = 0.3512$, 0.4309, and 0.5262 nm, which correspond to phase I, phase II, and phase III, respectively. The lowest

energy minimum, i.e., the most-stable phase, is phase II at $b = 0.4309$ nm. Phase I and phase III are metastable. The transition between phase I and phase II happens at $b = 0.3703$ nm, and the transition between phase II and phase III happens at $b = 0.5226$ nm. Note the discontinuity of the interlayer spacing d_1 at the given phase transition point. For phase III, d_1 becomes zero, i.e., two MLs merge into one monatomic layer. The energy barriers for phase transitions can be obtained from the μ values listed in Table S1.

For 3-ML Bi film (see Fig. 4c), we find three energy minima at $b = 0.3437$, 0.3737, and 0.5353 nm, which correspond to phase I, phase II, and phase III, respectively. The lowest energy minimum, i.e., the most-stable phase, is phase I at $b = 0.3437$ nm. Phase II and phase III are metastable. The transition between phase I and phase II happens at $b = 0.3580$ nm, and the transition between phase II and phase III happens at $b = 0.4853$ nm. Note the discontinuities of the interlayer spacings $d_1 \approx d_2$ at the given phase transition point. For large b, d_1 and d_2 become zero, i.e., three MLs merge into one monatomic layer. The energy barriers for phase transitions can be obtained from the μ values listed in Table S1.

For 4-ML Bi film (see Fig. 4d), we find three energy minima at $b = 0.3453$, 0.4425, and 0.5414 nm, which correspond to phase I, phase II, and phase III, respectively. The lowest energy minimum, i.e., the most-stable phase, is phase II at $b = 0.4425$ nm. Phase I and phase III are metastable. The transition between phase I and phase II happens at $b = 0.3628$ nm, and the transition between phase II and phase III happens at $b = 0.5189$ nm. Note the discontinuities of the interlayer spacings $d_1 \approx d_3$ and d_2 at the given phase transition point. For large b, d_2 become zero, i.e., two MLs in the middle merge into one monatomic layer. The energy barriers for phase transitions can be obtained from the μ values listed in Table S1.

As indicated by each red dash-dotted vertical line in Fig. 4, the equilibrium lattice parameters $b_{2\mathrm{ML}} = 0.4309$ nm and $b_{4\mathrm{ML}} = 0.4425$ nm for the most stable phases of 2- and 4-ML slabs are much closer to the bulk value $a = b_{\infty\mathrm{ML}} = 0.4580$ nm than $b_{1\mathrm{ML}} = 0.3304$ nm and $b_{3\mathrm{ML}} = 0.3437$ nm for the most-stable phases of 1- and 3-ML slabs, respectively. Not that $b_{1\mathrm{ML}} \approx b_{3\mathrm{ML}}$, while $b_{2\mathrm{ML}} \approx b_{4\mathrm{ML}} \approx b_{\infty\mathrm{ML}} = 0.4580$ nm $= a \approx a_0$, i.e., the lattice of an even-L Bi film almost perfectly matches the InSb(111) lattice with a_0.

The range of b in Fig. 4 is from 0.3 to 0.7 nm for Bi films or from 0.25 to 0.7 nm for Bi chain. This range is sufficiently large for identifying all possible phases (i.e., all energy minima), as rationalized below. For the side of small b, when $b < 0.3$ nm for Bi films and $b < 0.25$ nm for Bi chain, the energies are expected to monotonically and dramatically increase with decreasing b due to the gradually reduced NN distance of Bi atoms. Then, there would be no energy minima if $b < 0.3$ nm for Bi films or $b < 0.25$ nm for Bi chain. For the side of large b, 1-, 2-, or 3-ML Bi film or Bi chain approaches to the gas phase (with the chemical potential μ approaching to zero) with increasing b beyond 0.7 nm due to the too large NN distance of Bi atoms. Then, there would be no energy minima when $b > 0.7$ nm for 1-, 2-, or 3-ML Bi film or Bi chain. For 4-ML Bi, one more phase possibly occurs beyond $b > 0.7$ nm when d_1 and d_3 also become zero besides d_2 becomes zero (i.e., four Bi MLs become a monatomic layer). However, this is a trivial result. Finally, we find that 2-, 3-, and 4-ML Bi films are all nonmagnetic in the range of b from 0.3 to 0.7 nm.

In Table S1, we list our DFT optimized geometric and energetic properties of freestanding Bi structures including dimer, infinite chain, and 1- to 4-ML laterally infinite slabs with the thicknesses $L = 1, 2, 3,$ and 4. For a dimer, we take the k mesh to be $1 \times 1 \times 1$. For the chain, we use a supercell containing one Bi atom with the k mesh of $40 \times 1 \times 1$. For the 1- to 4-ML slabs, we fully relax a 1×1 supercell containing L Bi atoms with the k mesh of $41 \times 41 \times 1$. To obtain the multiple possible phases for a given b, we try different initial interlayer spacings d_1, d_2, and/or d_3.

Table S1. Optimized geometric and energetic properties of freestanding Bi structures from our DFT calculations. For calculation details and structure of bulk Bi crystal, see Sec. S3.1 and Fig. S1. b is the lateral lattice parameter for a low dimensional structure and $b = a$ for bulk Bi. d_1, d_2, and d_3 are the interlayer spacings counted from bottom to top layers for a Bi slab, respectively. For bulk, d_1 and d_2 are two adjacent interlayer spacings and $d = d_1 + d_2$, as shown in Fig. S1. Note that $d_1 = d_3$ for bulk and $d_1 \approx d_3$ for a 4-ML Bi slab for fully relaxed structures from our DFT calculations. All lengths are in units of nm. γ is the surface energy (in eV/nm^2) of a phase for a slab at the thickness L. $\Delta^2 E_L$ (in eV) is the second difference of the energy for the most-stable phase at L from two *most-stable* phases at the adjacent thicknesses $L-1$ and $L+1$. μ (in eV) is the chemical potential calculated by $\mu = E_{\text{cell}}/n - E_{\text{Bi}}$, where E_{cell} is the DFT total energy of the supercell containing n Bi atoms and E_{Bi} is the energy of one Bi atom in gas phase. The lowest μ for a given L indicates the most-stable phase (bold font). By taking the difference of two μ values (listed in last column) at adjacent energy extrema (see Fig. 4), one can obtain the energy barriers between two adjacent phases, e.g., the energy barrier is $-2.582 - (-2.528) = 0.054$ eV/atom from phase I to phase II for a 2-ML slab. For bulk, the chemical potential equals the minus cohesive energy, i.e., $\mu = -E_{\text{c}}$. The bottommost row lists experimental values of bulk Bi for a comparison.

Bi structure	L	b	d_1	d_2	d_3	d	γ	$\Delta^2 E_L$	μ
Dimer		0.2654							−1.627
Chain		0.2865							−1.638
1 ML	1	0.3304					4.091		−2.241
2 ML (phase I)	2	0.3512	2.6773				4.049		−2.582
2 ML (transition I ↔ II)	2	0.3703	2.4954						−2.528
2 ML (phase II)	2	0.4309	0.1751				1.654	+0.929	−2.748
2 ML (transition II ↔ III)	2	0.5226	0.0000						−2.280
2 ML (phase III)	2	0.5262	0.0000				3.055		−2.282
3 ML (phase I)	3	0.3437	0.2992	0.2989		0.5982	5.961	−1.268	−2.608
3 ML (transition I ↔ II)	3	0.3580	2.7034	2.7044		5.4078			−2.595
3 ML (phase II)	3	0.3737	0.2480	0.2478		0.4957	5.106		−2.603
3 ML (transition II ↔ III)	3	0.4853	1.5642	1.5657		3.1299			−2.191
3 ML (phase III)	3	0.5353	0.0875	0.0881		0.1756	3.797		−2.386
4 ML (phase I)	4	0.3453	0.2876	0.3348	0.2875	0.6224	6.227		−2.693
4 ML (transition I ↔ II)	4	0.3618	2.5427	3.0628	2.5443	5.6055			−2.670
4 ML (phase II)	4	0.4425	0.1699	0.2611	0.1699	0.4310	1.885		−2.855
4 ML (transition II ↔ III)	4	0.5189	0.7341	1.7369	0.7356	2.4710			−2.544
4 ML (phase III)	4	0.5414	0.0702	0.1661	0.0699	0.2363	3.333		−2.591
∞ ML (α-As phase)	∞	0.4580	0.1640	0.2379	0.1640	0.4019			−3.014
Experiments (α-As phase)	∞	0.4546[a]	0.1595[a]	0.2359[a]	0.1595[a]	0.3954[a]			−2.18[b]

[a]Refs. [66,67].
[b]Ref. [57].

Table S2. Dependences of optimized energies for C1, C2, and C3 relative to C0 on substrate lattice parameter l (for stable phases; see Table S1) and spring parameter k_1. The strain ε indicates the mismatch between substrate and 1-ML Bi with the equilibrium lattice parameter $b = 0.3304$ nm (see Table S1) from Eq. (5). Other parameters are the same as those listed in the caption of Fig. 3. A positive (negative) energy difference in columns 5, 6, and 7 for a configuration (C1, C2, or C3) indicates that this configuration is more unfavorable (favorable) than C0. The case with bold font corresponds to Fig. 3.

Substrate	l (nm)	ε	k_1 (eV/nm²)	$E_{C1} - E_{C0}$ (eV)	$E_{C2} - E_{C0}$ (eV)	$E_{C3} - E_{C0}$ (eV)	Favorability order
InSb(111)	0.45816	38.67%	500	+1.845	+3.418	+1.103	C0 > C3 > C1 > C2
			307	**+1.707**	**+3.460**	**+2.078**	**C0 > C1 > C3 > C2**
			10	−0.321	−0.492	+7.308	C2 > C1 > C0 > C3
2-ML Bi	0.4309	30.42%	500	+1.101	+2.053	+1.832	C0 > C1 > C3 > C2
			307	+1.019	+2.085	+2.434	C0 > C1 > C2 > C3
			10	−0.245	−0.374	+5.482	C2 > C1 > C0 > C3
3-ML Bi	0.3437	4.03%	500	−0.112	−0.166	+1.409	C2 > C1 > C0 > C3
			307	−0.113	−0.165	+1.411	C2 > C1 > C0 > C3
			10	−0.140	−0.209	+1.276	C2 > C1 > C0 > C3
4-ML Bi	0.4425	33.93%	500	+1.397	+2.596	+1.573	C0 > C1 > C3 > C2
			307	+1.293	+2.632	+2.323	C0 > C1 > C3 > C2
			10	−0.275	−0.420	+6.229	C2 > C1 > C0 > C3
∞-ML Bi	0.4546	37.59%	500	+1.738	+3.222	+1.222	C0 > C3 > C1 > C2
			307	+1.608	+3.263	+2.144	C0 > C1 > C3 > C2
			10	−0.316	−0.474	+7.056	C2 > C1 > C0 > C3

S3.3. Estimates of ϕ for chain and 1-ML Bi

For C0, C1, and C2 in Fig. 3, we take [47] $\phi = \phi_{1ML} = (E_{cell} - E_{Bi})/3 = -0.747$ eV, where E_{cell} is the DFT total energy of the 1-ML unit cell containing one Bi atom. For C3 in Fig. 3, we take $\phi = \phi_{chain} = E_{cell} - E_{Bi} = -1.638$ eV, where E_{cell} is the DFT total energy of the chain unit cell containing one Bi atom. Because of the simplicity of our proposed model, in principle, ϕ is an adjustable parameter which would depend on substrate [60,61], but we ignore any substrate effect in the above ϕ values.

S3.4. Estimates of k_1 and k_2 for chain and 1-ML Bi

We estimate k_2 from the DFT calculations of the total energy as a function of lattice parameter, e.g., for a 1-ML Bi or a Bi chain. From the energy curve, we can obtain the coefficient C of the quadratic term by fitting the curve using a quadratic polynomial and then we take $k_2 = 2C$. For C0, C1, and C2, we take $k_2 = k_{1ML} = 766$ eV/nm² from the 1-ML calculation. For C3, we take $k_2 = k_{chain} = 814$ eV/nm² from the chain calculation. These two values are different, but the difference between them is not very significant. Similar to the above ϕ value, k_2 is in principle also an adjustable parameter which would depend on substrate, but we ignore any substrate effect in the above k_2 values.

k_1 is another adjustable parameter, significantly depending on the property of the substrate. However, to experimentally determine an unambiguous structure of the wetting

layer of the substrate is inaccessible. In our proposed model, we assume that the substrate wetting layer has the triangular lattice which is the same as InSb(111) plane and the wetting layer is made up of intermixed Bi, Sb, and In atoms. For such a system, the DFT calculations are demanding. As a rough estimate for an order of magnitude, we just consider one Bi atom adsorbed on a 3×3 frozen 1-ML Bi and calculate the total energy as a function of the distance from the equilibrium site of the Bi atom. Then we can obtain the coefficient C of the quadratic term by fitting the curve using a quadratic polynomial and then we obtain $k_1 = k_{\text{sub}} = 2C = 307$ eV/nm^2. It should be mentioned that this very roughly estimated value is not necessarily the real value because the result sensitively depends on the positions near the equilibrium site of the Bi atom, and it is also very likely that k_1 also sensitively depends on the thickness of a Bi film as the substrate. About the uncertainty of k_1, further analysis is as below.

To support the above estimates of k_1 and k_2 values from our DFT calculations, we also make an estimate simply using the dispersion relation $\omega_{\text{max}} = 2\sqrt{k/m}$ for a one-dimensional atom chain, where m is the mass of one atom, and the maximum vibration frequency ω_{max} can be estimated from the Debye frequency $\omega_{\text{D}} = k_{\text{B}}\Theta_{\text{D}}/\hbar$ with the Boltzmann constant k_{B} and the Debye temperature Θ_{D}. For Bi, $\Theta_{\text{D}} = 119$ K [57], and then the estimated value of the spring parameter k is about 131 eV/nm^2, which is in the same order of magnitude as the above ranges of DFT values of k_1 and k_2. For different materials, e.g., single-element materials [57], Θ_{D} varies over a wide range from 38 K for Cs to 2230 K for C, and then k can vary from 1 to 10^3 eV/nm^2 in order of magnitude correspondingly. This feature increases the uncertainties in determining these spring parameters. In particular, k_1 would sensitively depend on the material property of substrate, e.g., from the InSb surface (wetting layer) to the 2-ML Bi film and then to the thicker 4-ML Bi film as the substrate in this work. Thus, as listed in Table S2, we take multiple k_1 values: 10, 307, and 500 eV/nm^2, which can be viewed as three typical k_1 values within the above range of the order of magnitude from about 1 to 10^3 eV/nm^2 in our model analyses. This implies that, although we take the value of $k_1 = 307$ eV/nm^2 from the above DFT estimate for a model analysis in Fig. 3, the real k_1 would significantly differ from this value.

As emphasized above, k_1 is treated as an adjustable parameter due to its uncertainties. Nevertheless, we expect that the bottommost InSb substrate would have relatively strong interactions with 1-ML Bi on the wetting layer (and therefore k_1 would be relatively large in this case); the interactions would be still significant for 2-ML Bi on the wetting layer (and therefore k_1 would be still relatively large) due to the top Bi adlayer is still sufficiently close to InSb, but the interactions would become insignificant for Bi films larger than 3 MLs on the wetting layer (and therefore k_1 would become significantly smaller) due to the top Bi adlayer is far away from InSb.

S3.5. Notes for 2-ML Bi film exhibiting (2×2)-reconstruction-like regions

During the cooling or annealing time, Level 2 can exhibit either disordered morphologies (Fig. S6b,f) or (2×2)-reconstructed-like surface [the (2×2)-like periodicity is indicated by a rhombus with the measured side length of about $2a$ in Fig. S6d, where a is the lattice constant of Bi(111) plane]. Also, Level 2 in Fig. S4e,f shows a mixture of disordered and (2×2)-reconstruction-like morphologies. As for why the 2-ML Bi film can

exhibit a (2×2)-reconstruction-like surface (Level 2) on the substrate, we hypothesize that a (2×2)-reconstruction-like surface could be more favorable energetically than an unreconstructed surface for a 2-ML Bi film on the InSb substrate. We believe that a model analysis similar to that for the 1-ML islands described in the main text is straightforward with an appropriately modified set of parameters. However, the analysis can be much more complicated because our experimental imaging cannot resolve the structural details of a (2×2)-reconstruction-like region. (One possibility is that the top Bi atoms become nonuniform, e.g., each light dot in a Level 2 area probably corresponds to a Bi trimer.)

As seen in Fig. S6, after a long annealing time, the ST-like structures (Level S_1 and Level S_3) evolve into the superstable Level 2 (the 2-ML Bi film). This indicates that the ST-like structures have higher surface energies but are metastable relative to Level 2 and occur due to inhibited interlayer transport during film growth. The ST-like structures are expected to have significant energy barriers towards the superstable Level 2. To overcome the barriers, the long annealing time at higher temperature is needed.

S3.6. Stability analysis for Bi films with different thicknesses

To determine the stability of a slab with the thickness L, the surface energy γ of the slab is calculated from [47]

$$\gamma = \frac{E_{\text{cell}} - n\sigma_{\text{bulk}}}{2A}, \tag{6}$$

where E_{cell} is the total energy of the supercell, n is the number of Bi atoms in the supercell, A is the area of one of two free faces of the supercell, and σ_{bulk} is the energy per Bi atom in bulk Bi crystal. The second difference of the energy at L is [47]

$$\Delta^2 E_L = E_{L+1} + E_{L-1} - 2E_L, \tag{7}$$

which is used to determine the stability of a film with the thickness L during the thin film growth [47]. E_{L-1}, E_L, and E_{L+1} are the E_{cell} values at $L-1$, L, and $L+1$, respectively. Relative to $L+1$ and $L-1$, a large positive value of $\Delta^2 E_L$ indicates high stability of the film with L, and a negative value indicates that the film with L is unstable. Also note that using Eq. (7) to determine the stability can avoid the calculation of an extra quantity of σ_{bulk} in Eq. (6). From Table S1, the surface energy $\gamma_{L=3} = 5.961$ eV/nm^2 for the most-stable phase I of 3-ML film is significantly higher than $\gamma_{L=1} = 4.091$ eV/nm^2 for 1-ML film, $\gamma_{L=2} = 1.654$ eV/nm^2 for the most-stable phase II of 2-ML film, and $\gamma_{L=4} = 1.885$ eV/nm^2 for the most-stable phase II of 4-ML film. The corresponding second difference of the energy for a 3-ML slab (phase I) is $\Delta^2 E_{L=3} = -1.268$ eV < 0. The highest surface energy and the negative second energy difference indicate that a 3-ML slab is unstable, relative to other thicknesses, where the 2-ML slab (phase II) is most stable with the lowest surface energy and positive $\Delta^2 E_{L=2} = +0.929$ eV > 0. The order of stabilities for different slab thicknesses L at their most-stable phases based on the surface energies is $L = 2$ (phase II), 4 (phase II), 1, and 3 (phase I). In addition, the lattice of an even-L Bi film ($L = 2$ or 4) almost perfectly matches the InSb(111) lattice with a_0, but not for an odd-L Bi film ($L = 1$ or 3). Thus, 2- and 4-ML compact Bi films should have higher occurrence rates than 1- and 3-ML compact Bi films. This is reasonably consistent with our experimental results, for which 2-ML Bi film (Level 2) and 4-ML Bi film (Level 4) are observable (4-ML Bi film has a very low occurrence rate

relative to 2-ML film because of $\gamma_{L=4} > \gamma_{L=2}$), while 1- and 3-ML compact Bi films are unobservable because of much higher surface energies (instead, the 1-ML ST Bi on wetting layer or on 2-ML Bi film has very high occurrence, analyzed from the model in Sec. 2).

As shown in Fig. 4, except phase II for 3-ML film, the total energies (or chemical potentials μ) as well as surface energies γ of all other metastable phases for 2-, 3-, and 4-ML films are significantly higher than their most-stable phases. In addition, the lattice of anyone of these metastable phases has a significant mismatch with the InSb(111) lattice, as listed in Table S1. Then, we expect that the probabilities that the structures corresponding to these metastable phases for freestanding Bi films are observed in experiments (with the substrate) would be very low. The energy of phase II for 3-ML film is close to that of phase I, but their d_1 values are also very close, i.e., these two phases are almost degenerate. Thus, in our analysis, we only consider the most-stable phase for the film with any thickness.

S3.7. Electronic topological properties of Bi films with different thicknesses

We first calculate the band structures of *freestanding* 1-, 2-, 3-, and 4-ML Bi films for their most-stable phases listed in Table S1. The supercell has a lateral size of 1×1. Because the calculations including SOC are demanding and very accurate values are not necessary for our purpose, we reduce the k mesh to $12 \times 12 \times 1$ and reduce the energy cutoff to be 450 eV. From our DFT results, 1- and 3-ML Bi films are metallic without a global gap, while 2- and 4-ML Bi films have topological gaps, i.e., odd- and even-L Bi films are topologically trivial and nontrivial, respectively. Thus, our DFT result for electronic topological properties of 2- and 4-ML Bi films is consistent with the previous prediction [35,36]. To simulate a non-periodic ST film with a periodic supercell in our DFT calculations, we use a 5×5 supercell cell (and a k mesh of $6 \times 6 \times 1$) with a vacancy where one Bi atom (seven Bi atoms) is (are) removed, corresponding to a Bi coverage of 0.4 (0.28) ML, versus the coverage of about 0.8 ML for a ST film like that in Fig. 2d. From the band structure analysis with the Wannier functions [35,36], we find that the configurations for a 1-ML film with the vacancies and for a 1-ML film with the vacancies on a 2-ML film are still topologically trivial (like an odd-L film), i.e., the electronic topology of a 2-ML film can be turned off by growing a ST ML on it.